



Article

Signatures of Electric Field and Layer Separation Effects on the Spin-Valley Physics of MoSe₂/WSe₂ Heterobilayers: From Energy Bands to Dipolar Excitons

Paulo E. Faria Junior * and Jaroslav Fabian

Institute for Theoretical Physics, University of Regensburg, 93040 Regensburg, Germany

* Correspondence: paulo-eduardo.faria-junior@ur.de or fariajunior.pe@gmail.com

Abstract: Multilayered van der Waals heterostructures based on transition metal dichalcogenides are suitable platforms on which to study interlayer (dipolar) excitons, in which electrons and holes are localized in different layers. Interestingly, these excitonic complexes exhibit pronounced valley Zeeman signatures, but how their spin-valley physics can be further altered due to external parameters—such as electric field and interlayer separation—remains largely unexplored. Here, we perform a systematic analysis of the spin-valley physics in MoSe₂/WSe₂ heterobilayers under the influence of an external electric field and changes of the interlayer separation. In particular, we analyze the spin (S_z) and orbital (L_z) degrees of freedom, and the symmetry properties of the relevant band edges (at K, Q, and Γ points) of high-symmetry stackings at 0° (R-type) and 60° (H-type) angles—the important building blocks present in moiré or atomically reconstructed structures. We reveal distinct hybridization signatures on the spin and the orbital degrees of freedom of low-energy bands, due to the wave function mixing between the layers, which are stacking-dependent, and can be further modified by electric field and interlayer distance variation. We find that H-type stackings favor large changes in the g-factors as a function of the electric field, e.g., from -5 to 3 in the valence bands of the H_h¹ stacking, because of the opposite orientation of S_z and L_z of the individual monolayers. For the low-energy dipolar excitons (direct and indirect in k -space), we quantify the electric dipole moments and polarizabilities, reflecting the layer delocalization of the constituent bands. Furthermore, our results show that direct dipolar excitons carry a robust valley Zeeman effect nearly independent of the electric field, but tunable by the interlayer distance, which can be rendered experimentally accessible via applied external pressure. For the momentum-indirect dipolar excitons, our symmetry analysis indicates that phonon-mediated optical processes can easily take place. In particular, for the indirect excitons with conduction bands at the Q point for H-type stackings, we find marked variations of the valley Zeeman (~ 4) as a function of the electric field, which notably stands out from the other dipolar exciton species. Our analysis suggests that stronger signatures of the coupled spin-valley physics are favored in H-type stackings, which can be experimentally investigated in samples with twist angle close to 60°. In summary, our study provides fundamental microscopic insights into the spin-valley physics of van der Waals heterostructures, which are relevant to understanding the valley Zeeman splitting of dipolar excitonic complexes, and also *intralayer* excitons.

Keywords: valley Zeeman; spin-valley; van der Waals heterostructure; TMDC

Citation: Faria Junior, P.E.; Fabian, J. Signatures of Electric Field and Layer Separation Effects on the Spin-Valley Physics of MoSe₂/WSe₂ Heterobilayers: From Energy Bands to Dipolar Excitons. *Nanomaterials* **2023**, *13*, 1187. <https://doi.org/10.3390/nano13071187>

Academic Editor: Maciej Molas

Received: 28 February 2023

Revised: 22 March 2023

Accepted: 24 March 2023

Published: 27 March 2023



Copyright: © 2023 by the authors. Licensee MDPI, Basel, Switzerland. This article is an open access article distributed under the terms and conditions of the Creative Commons Attribution (CC BY) license (<https://creativecommons.org/licenses/by/4.0/>).

1. Introduction

Transition metal dichalcogenides (TMDCs) monolayers host a plethora of fascinating physical properties: for instance, these materials are direct band gap semiconductors with strong spin-orbit coupling (SOC) [1–5], and display robust signatures of excitonic and valley contrasting physics [6–14]. Furthermore, the van der Waals nature of TMDC materials facilitates the vertical stacking and integration of different layers, the key ingredient driving the burgeoning research field of van der Waals heterostructures [15–18].

These novel heterostructures offer a fantastic playground in which to investigate the emergent physical phenomena and effects of proximity interaction, which is certainly not limited to TMDCs [19–22], but also encompasses other attractive materials, such as graphene [13,23–27], boron nitride [28–30], ferromagnetic CrX_3 ($X = \text{I, Br}$) [31–35], and many others.

In particular, for the TMDC-based van der Waals heterostructures, one relevant system of great interest is the $\text{MoSe}_2/\text{WSe}_2$ heterobilayer: in this system, the type-II band alignment favors the appearance of interlayer excitons, also known as dipolar excitons, with electrons and holes localized in different layers [36–38]. Interestingly, dipolar excitons exhibit long recombination times [39–41], robust out-of-plane electric dipole moments [42–46], and giant valley Zeeman signatures that are dependent on the twist angle and atomic registry [20,43,47–51]: these are attractive features that could be exploited in exciton-based opto-spintronics devices [17,18], such as dipolar excitons quantum emitters [43] and diode transistors [46]. Furthermore, these $\text{MoSe}_2/\text{WSe}_2$ are suitable platforms on which to study the optical signatures of moiré superlattices [19,20,52,53] and atomic reconstruction [54–57]. From a fundamental perspective, there is still some debate about the energy bands that constitute these dipolar excitons. A few reports suggest momentum-indirect dipolar excitons originating from valence bands at the K point and conduction bands at the Q point [40,58,59], despite the strong evidence of momentum-direct dipolar excitons with conduction and valence bands located at the K point [20,47–51,60,61] with a distinct valley Zeeman signature of ~ -16 . Interestingly, it has recently been shown that these different dipolar exciton species exhibit different electric dipole moments [45], thus providing a possible alternative with which to properly distinguish them under applied electric fields. In order to fully exploit the functionalities of dipolar excitons in van der Waals heterostructures, it is particularly important to understand their spin-valley physics, and how they depend on external parameters, such as applied electric fields [36,62] and fluctuations of the interlayer distance [63].

In this manuscript, we employ first-principles calculations, to study the spin-valley physics of $\text{MoSe}_2/\text{WSe}_2$ heterostructures, focusing on high-symmetry stackings with 0° (R-type) and 60° (H-type) twist angle under the influence of external electric fields and variations of the interlayer distance. We perform a systematic analysis of the spin (S_z) and orbital (L_z) angular momenta, g-factors, and symmetry properties of the relevant band edges (at K, Q, and Γ points), and reveal that different stackings imprint distinct hybridization signatures on the spin-valley physics of these low-energy bands. We follow the successful framework for computing the valley Zeeman splitting in TMDC materials [64–67], in which atomistic and “valley” contributions are correctly taken into account via the orbital angular momentum of the Bloch function. We extend our analysis to investigate direct- and indirect-in-momentum dipolar (interlayer) excitons, revealing that different exciton species present distinct electric dipole moments, polarizabilities, and g-factors. In particular, direct dipolar excitons in the K-valley hold a robust valley Zeeman splitting nearly independent of the electric field, whereas momentum-indirect dipolar excitons, with conduction bands at the Q point, show a clear dependence of the valley Zeeman splitting on the positive values of applied electric fields (with variations of ~ 4). The dipolar exciton g-factors can also be affected by varying the interlayer distance, which could be experimentally probed under external pressure. Because of the opposite orientation of S_z and L_z of the individual monolayers, our results reveal that changes in the valley Zeeman, due to electric field or interlayer distance, are more pronounced in H-type systems, such as the g-factor variation from -5 to 3 in the valence bands of the H_h^h stacking. These pronounced valley Zeeman signatures should be experimentally accessible in samples with a twist angle close to 60° , which give rise to moiré or atomic reconstructed domains dominated by the high-symmetry H-type stackings.

This manuscript is organized as follows: in Section 2, we discuss the electronic structure and symmetry properties of the studied R- and H-type high-symmetry stackings; in Section 3, we explore the spin-valley physics of the relevant band edges, and how they are affected by

an applied electric field and variations of the interlayer distance; in Section 4, we focus on the direct and indirect, in k -space, dipolar excitons originated from the low-energy band edges; we discuss their selection rules, based on symmetry analysis and first-principles calculations, their valley Zeeman signatures (effective g -factors), and how the effect of external electric fields and variations of the interlayer distance impact the optical selection rules and valley Zeeman physics; finally, in Section 5, we summarize our findings, and place our study in the broader context of the growing research field of valleytronics in multilayered van der Waals heterostructures.

2. General Features of MoSe₂/WSe₂ High-Symmetry Stackings

We focus on artificially stacked MoSe₂/WSe₂ heterostructures with relative angles of 0° (R-type) and 60° (H-type). When the individual MoSe₂ and WSe₂ layers are stacked together, the angle is not precisely 0° or 60°, and the small misalignment can give rise to moiré superlattices or atomic reconstruction [19,20,52–57], with length scales of tens of nm. However, either in the moiré or in the atomic reconstruction perspective, there are distinct contributions from well-defined high-symmetry stackings that dominate the observed properties [20,64,68–70], such as the dipolar excitons selection rules and g -factors. Furthermore, these high-symmetry stackings also serve as building blocks for the effective modeling of interlayer moiré excitons [68,69,71–75].

Side-views of the considered high-symmetry stackings (R_h^h , R_h^M , R_h^X , H_h^h , H_h^M , and H_h^X) are shown as insets in Figure 1a–f, and we follow the labeling of Refs. [19,64]. To clarify, the stacking label X_b^a indicates the twist angle $X = R$ (0°) or $X = H$ (60°) and relative shifts between the bottom (subscript a) and top (superscript b) layers, with a,b = h (hollow), M (metal), and X (chalcogen). For instance, the R_h^X stacking indicates a structure with 0°, with the chalcogen atom of the top layer positioned on top of the hollow position of the bottom layer. To construct the heterostructure, we start with the values of the in-plane lattice parameter (a) and the thickness (t) of the individual monolayers, given by $a = 3.289$ Å, $t = 3.335$ Å for MoSe₂, $a = 3.282$ Å, $t = 3.340$ Å for WSe₂, taken from Ref. [76]. For the MoSe₂/WSe₂ heterostructures, we consider an average lattice parameter of $a = 3.2855$ Å, leading to an average strain of ~0.1%. We also correct the monolayer thickness due to strain [77], leading to $t = 3.3375$ Å and $t = 3.3374$ Å for MoSe₂ and WSe₂, respectively. A vacuum region of 20 Å is considered for all cases. The equilibrium interlayer distances, d , are given in Table 1, and are consistent with several reports in the literature [19,37,38,64,78–80]. We also present, in Table 1, the effective distance between Mo and W atoms. We perform our first-principles calculations based on the density functional theory (DFT), as implemented in the WIEN2k [81] code, with details given in Appendix A.

Table 1. Interlayer distance, d , and effective Mo-W distance for the studied R- and H-type systems.

	R_h^h	R_h^M	R_h^X	H_h^h	H_h^M	H_h^X
d (Å)	3.7237	3.0803	3.0869	3.0923	3.6885	3.1833
Mo-W (Å)	7.0612	6.6922	6.6985	6.7037	7.2775	6.5208

The layer-resolved band structures for all the calculated R- and H-type structures are shown in Figure 1a–f. We are particularly interested in the band edges that can host dipolar excitons (K, Q, and Γ points), as depicted in Figure 1g, and how they are affected by external electric fields and changes of the interlayer distance, schematically shown in Figure 1h. The conduction and top valence bands at the K point are highly layer-localized, and maintain the same order, regardless of the stacking (bands $c_{W\pm}$, $c_{M\pm}$, v_W , and v_M). On the other hand, the ordering of the lowest valence bands depends on the particular stacking (therefore, we identify them as just v_+ and v_- , specifying the majority layer composition when necessary). The energy bands outside of the K point often show a higher interlayer hybridization, as is the case of the low-energy conduction bands at the Q point ($c_{Q\pm}$), and the top valence band at the Γ point (v_Γ). Because of the different twist angle

(0° or 60°) between the layers, the relative spin degree of freedom is certainly affected, as indicated by the spin-resolved band structure shown in Figure 2.

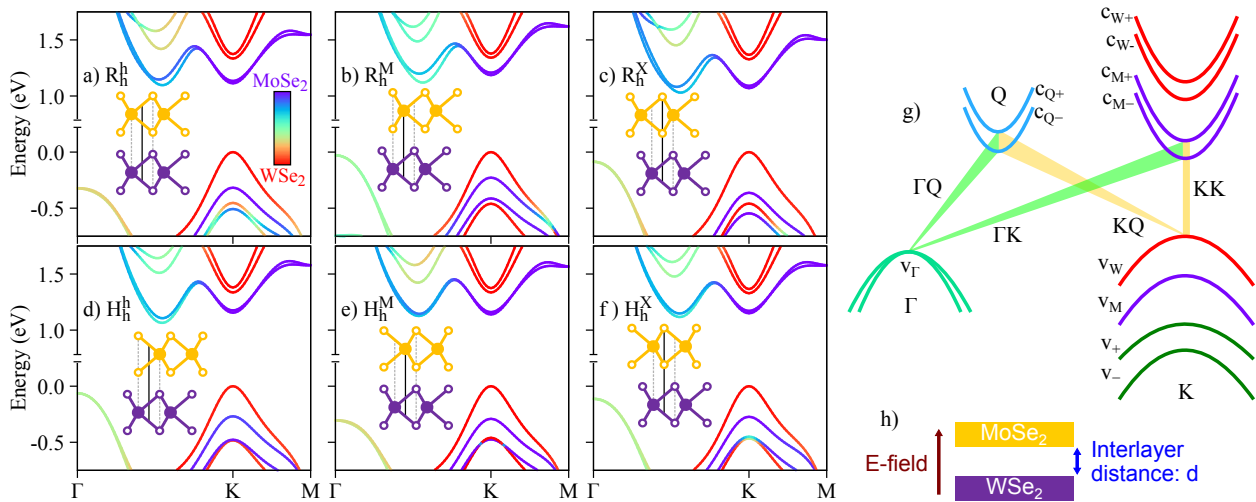


Figure 1. (a–f) calculated band structures, with the color-coded layer decomposition of the wave function for (a) R_h^h , (b) R_h^M , (c) R_h^X , (d) H_h^h , (e) H_h^M , and (f) H_h^X stackings; the insets show the side-view of the crystal structures (solid lines connect the hollow position of the bottom layer to the atomic registry of the top layer); (g) relevant low-energy bands and possible interlayer exciton transitions originating from the top valence bands at the Γ (v_Γ) and K points (v_W); the transitions involving the time-reversal partners ($-K$ and $-Q$ points) are not shown, for simplicity; (h) schematic representation of the applied external electric field and the interlayer distance.

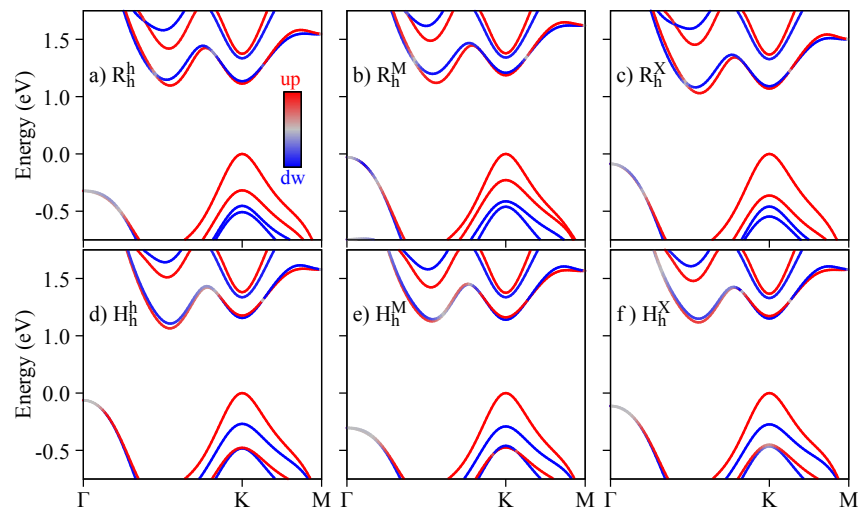


Figure 2. Spin-resolved band structures for the (a) R_h^h , (b) R_h^M , (c) R_h^X , (d) H_h^h , (e) H_h^M , and (f) H_h^X stackings.

In terms of symmetry, the R- and H-type structures considered belong to the C_{3v} ($P3m1$) point group. In reciprocal space, the symmetry group of the Γ point is also the C_{3v} group, and is reduced to its subgroups for other k -points. We find the C_3 group for the K point, the C_1 group for the Q point, and the C_s group for the M point. It is also relevant to identify the double-group (with SOC) irreducible representations (irreps) for the relevant energy bands shown in Figure 1g: these irreps are useful building blocks with which to study the allowed optical selection rules (direct and phonon-mediated), and possible (intra- and/or inter-valley) scattering mechanisms, as already studied in the monolayer cases [50,82–85]. Furthermore, irreps are crucial to building effective models within the $\mathbf{k}\cdot\mathbf{p}$ framework [76,86–90], in which additional symmetry-breaking terms can be easily incorporated. Specifically for the K point, the irreps of the energy bands are given

in Table 2. As the K_4 and K_5 irreps are complex, the irreps at $-K$ can be found by taking the complex conjugate $K_4 \rightarrow K_5 = K_4^*$, $K_5 \rightarrow K_4 = K_5^*$. The top valence band at the Γ point (2-fold degenerate) belongs to the (real) irrep Γ_4 of the C_{3v} group, and the lower conduction bands at the Q point both belong to the (real) irrep Q_2 of the C_1 group. To clarify our notation, we identify the irreps by their reciprocal space point, i.e., K_i irreps belong to the K point, Γ_i irreps for the Γ point, and Q_i irreps for the Q point. We also emphasize that the irreps are obtained using the full wave function calculated within DFT, as implemented in WIEN2k [81]. All the irreps and symmetry groups discussed here follow the character tables of Ref. [91].

Table 2. Irreducible representations at the K point (C_3 point group) for the relevant energy bands indicated in Figure 1g for all considered stackings.

	R_h^h	R_h^M	R_h^X	H_h^h	H_h^M	H_h^X
c_{W+}	K_5	K_6	K_4	K_4	K_6	K_5
c_{W-}	K_4	K_5	K_6	K_6	K_5	K_4
c_{M+}	K_4	K_4	K_4	K_5	K_5	K_5
c_{M-}	K_5	K_5	K_5	K_4	K_4	K_4
v_W	K_4	K_5	K_6	K_6	K_5	K_4
v_M	K_4	K_4	K_4	K_5	K_5	K_5
v_+	K_6	K_6	K_5	K_6	K_4	K_6
v_-	K_6	K_4	K_6	K_5	K_6	K_6

3. Spin-Valley Physics at the Band Edges

3.1. Pristine Heterostructures

In this section, we explore the spin and orbital degrees of freedom for the relevant band edges (indicated in Figure 1g) at zero electric field and at the equilibrium interlayer distance. We follow recent first-principles developments, to compute the orbital angular momenta in monolayer TMDCs [64–67], which has also been successfully applied to investigate a variety of more complex TMDC-based systems and van der Waals heterostructures [27,53,57,80,85,92–99]. We do not aim to provide a detailed description of the methodology here, but briefly summarize the main points. An external magnetic field in the out-of-plane (z) direction (same orientation as the electric field in Figure 1h) modifies the energy levels as

$$E_{ZS}(n, \vec{k}) = g_z(n, \vec{k})\mu_B B = [S_z(n, \vec{k}) + L_z(n, \vec{k})]\mu_B B, \quad (1)$$

in which the g -factor, $g_z(n, \vec{k})$, of the Bloch band (labeled by n and \vec{k}) is written in terms of the spin and orbital angular momenta, given by

$$S_z(n, \vec{k}) = \langle n, \vec{k} | \sigma_z | n, \vec{k} \rangle$$

$$L_z(n, \vec{k}) = \frac{1}{im_0} \sum_{m \neq n} \frac{P_x^{n,m,\vec{k}} P_y^{m,n,\vec{k}} - P_y^{n,m,\vec{k}} P_x^{m,n,\vec{k}}}{E(n, \vec{k}) - E(m, \vec{k})}, \quad (2)$$

in which σ_z is the Pauli matrix for the spin components along z , $P_\alpha^{n,m,\vec{k}} = \langle n, \vec{k} | p_\alpha | m, \vec{k} \rangle$ ($\alpha = x, y, z$), \vec{p} is the momentum operator, $E(n, \vec{k})$ is the energy of the Bloch band, and m_0 is the free electron mass. In the expression of the spin angular momentum, we use $g_0 \approx 2$ for the electron spin g -factor. The summation-over-bands that characterizes L_z requires a sufficiently large number of bands (~ 500) to achieve convergence, which is properly taken into account in our DFT calculations (see details in Appendix A). These MoSe₂/WSe₂ heterostructures were investigated in Refs. [53,57,64,67,80] but here we extend our analysis to

incorporate more bands, and later investigate the dependence of electric field and inter-layer distance. We emphasize here that the electronic and spin properties calculated with the DFT also provide a reliable benchmark for further studies, as WIEN2k [81] is one of the most accurate DFT codes available [100], and is particularly suitable for studying the spin-physics of 2D materials and van der Waals heterostructures [23,24,27,95,101–105].

Our calculated values of S_z and L_z for the monolayers are collected in Table 3, and the results for the R- and H-type stackings are shown in Table 4. For the monolayer cases, we use the same in-plane lattice parameters and thicknesses as used in the heterostructure, so that we can directly compare the monolayer values of S_z and L_z to the heterostructure. The amount of strain of $\sim 0.1\%$ for the in-plane lattice parameter has a very small influence on the spin-valley physics of individual monolayer TMDCs [77,95], with contributions in the order of 10^{-2} from the unstrained values; therefore, any changes of $L_z > 10^{-2}$ are clear signatures of interlayer hybridization. For the heterostructure bands at the K point, $c_{W(Mo)\pm}$, $v_{W(Mo)}$, and v_{\pm} , we observe the typical sign changes from R to H stackings, because of the opposite K/K (0° twist) and K/ $-K$ (60° twist) alignment [20,64]. For the conduction bands, we observe deviations of L_z in the order of ≤ 0.05 , when compared to the monolayer case, consistent with a higher localization of conduction bands [27]. We therefore would expect larger changes arising in the valence bands, which is indeed the case, particularly for the v_{\pm} bands, and for the v_W and v_{Mo} bands of the H_h^h stacking. Furthermore, the effects of band mixing in the R stacking are less pronounced, because at zero field and at the equilibrium distance the values of L_z have the same sign and similar magnitude, whereas in the H stacking, L_z has the opposite sign, and any admixture of the energy bands can significantly alter L_z . For the highly delocalized bands at Γ and Q points, we find values of S_z and L_z that are in between the values of the individual $MoSe_2$ and WSe_2 monolayers, but still with $|S_z| > |L_z|$, thus making spin the dominant degree of freedom, as in the monolayer case [95]. The g_z values, g_z , can be found by adding S_z and L_z (we also present g_z graphically in the Sections 3.2 and 3.3, as a function of the electric field and interlayer distance).

Table 3. Calculated values of S_z and L_z for the relevant energy bands in monolayers.

	MoSe ₂		WSe ₂	
	S_z	L_z	S_z	L_z
c_+	−0.99	1.53	0.99	2.98
c_-	1.00	1.81	−0.89	1.88
v_+	1.00	3.94	1.00	5.02
v_-	−0.99	3.67	−0.98	4.07
v_Γ	0.96	0.06	0.87	0.19
c_{Q+}	−1.00	−0.09	−0.99	0.32
c_{Q-}	1.00	−0.16	0.96	0.05

Table 4. Calculated values of S_z and L_z for the relevant energy bands in R- and H- type stackings.

	R_h^h		R_h^M		R_h^X		H_h^h		H_h^M		H_h^X	
	S_z	L_z										
c_{W+}	0.97	2.98	0.97	3.02	0.97	2.97	0.97	2.92	0.97	2.98	0.97	3.02
c_{W-}	−0.88	1.88	−0.87	1.93	−0.88	1.88	−0.85	1.86	−0.89	1.89	−0.88	1.90
c_{M+}	−0.98	1.53	−0.98	1.55	−0.98	1.54	0.98	−1.54	0.98	−1.52	0.98	−1.56
c_{M-}	1.00	1.81	0.99	1.84	1.00	1.81	−1.00	−1.80	−1.00	−1.80	−1.00	−1.81
v_W	1.00	5.02	1.00	4.99	1.00	4.98	1.00	4.79	1.00	5.01	1.00	5.02
v_M	1.00	3.94	0.99	3.94	1.00	3.91	−1.00	−3.25	−1.00	−3.93	−1.00	−3.95
v_+	−0.98	4.04	−0.99	3.63	−0.98	4.01	0.99	−3.45	−0.98	4.08	0.24	−0.67
v_-	−0.99	3.70	−0.96	4.02	−0.99	3.62	−0.98	3.41	0.99	−3.66	−0.22	1.06
v_Γ	0.92	0.09	0.95	0.04	0.95	0.05	0.95	0.05	0.93	0.08	0.95	0.05
c_{Q+}	−0.93	0.11	−0.91	0.23	−0.87	0.14	−0.80	0.22	−0.59	0.12	−0.69	0.23
c_{Q-}	0.95	0.06	0.92	0.19	0.92	0.09	0.79	0.22	0.60	0.17	0.68	0.23

3.2. Electric Field Dependence

We now investigate the effect of external electric fields on the band edges of the R- and H-type stackings. In Figure 3, we show the energy dependence of the relevant energy bands (see Figure 1g) as a function of the electric field, with the color code of the K bands representing the layer-decomposition in the top row and the spin degree of freedom in the bottom row. Due to the particular symmetry of the energy bands (orbital and spin characters), the electric field can induce crossings or anti-crossings. The anti-crossings, visible in the top row of Figure 3 when the color code deviates from red (WSe₂ layer) or blue (MoSe₂ layer), indicate regions with strong interlayer hybridization; furthermore, these anti-crossings can either mix or preserve the spin degrees of freedom, depending on the stacking and bands involved. For instance, for the H_h^h stacking, there is an anti-crossing between v_M and v_- (mainly localized at the WSe₂ layer) that preserves spin. On the other hand, the anti-crossing of the R_h^M stacking between v_M and v_- (mainly localized at the WSe₂ layer) also acts on the spin degree of freedom. We point out that the conduction bands at the Q point, shown by short dashed lines, do not present any crossing when the energy levels get closer as the values of the electric field increase, as shown in the insets of Figures 3g–l. The crossing of conduction bands takes place when the electric field values are smaller than ~ -0.75 V/nm.

The electric field dependence of the quantities S_z , L_z , and g_z , which encode the essence of spin-valley physics, is summarized in Figures 4–6, respectively. The most important feature revealed by our calculations is that S_z , L_z , and g_z are strongly mixed around the anti-crossing regions shown in Figure 3. In other words, spin and orbital degrees of freedom provide a clear quantitative signature for the strength of the interlayer coupling in these van der Waals heterostructures. Let us discuss in detail the case of H_h^h stacking, which shows the most prominent anti-crossing region for the valence bands v_M and v_- . The orbital and spin analysis in Figure 3 reveal that v_M and v_- mix on the orbital level, while the spin remains unchanged. Indeed, by inspecting Figure 4j, we confirm that S_z is unchanged for the interval of the applied electric field. On the other hand, Figure 5j shows that the values of L_z are drastically modified as the electric field swipes through the anti-crossing region, with the strongest mixing happening at ~ 1.5 V/nm. In fact, already at zero electric field (as shown in Table 4), we clearly observe the hybridization effect taking place in the values of L_z , suggesting that small values of applied electric field are enough to tune this hybridization even more. We point out that there are anti-crossing signatures also taking place in the conduction band; however, it seems that this feature has not been observed experimentally, due to the range of electric field values applied [42,43,45]. Additionally, the electric field introduces a strong change of the spin character in the conduction bands at the Q point, due to their anti-crossing (insets of Figure 3g–l), an interesting feature that can be investigated in low-energy interlayer excitons [45], which we discuss in further detail in Section 4.3. We note that the field-driven Rashba SOC is naturally incorporated within our first-principles calculations; however, the electric field is just too weak to effectively remove spins from their out-of-plane direction.

Our detailed first-principles calculations reveal that the H_h^h stacking is the most suitable structure with which to investigate these interlayer hybridization signatures in the coupled spin-valley degrees of freedom. Surprisingly, this is the most stable structure for 60° twist angles, and the most relevant stacking for small twist angles, either having in mind a moiré or an atomically reconstructed sample, which facilitates the experimental accessibility to these effects. Furthermore, the opposite orientation of spin and orbital angular momenta from the opposite K-valleys in the individual monolayers favors g-factor variations from negative to positive values: for example, from -3 to 4 in the conduction band (Figure 6d), from -5 to 3 in the valence band (Figure 6j), and from -1 to 1 for conduction bands at the Q point (Figure 6p).

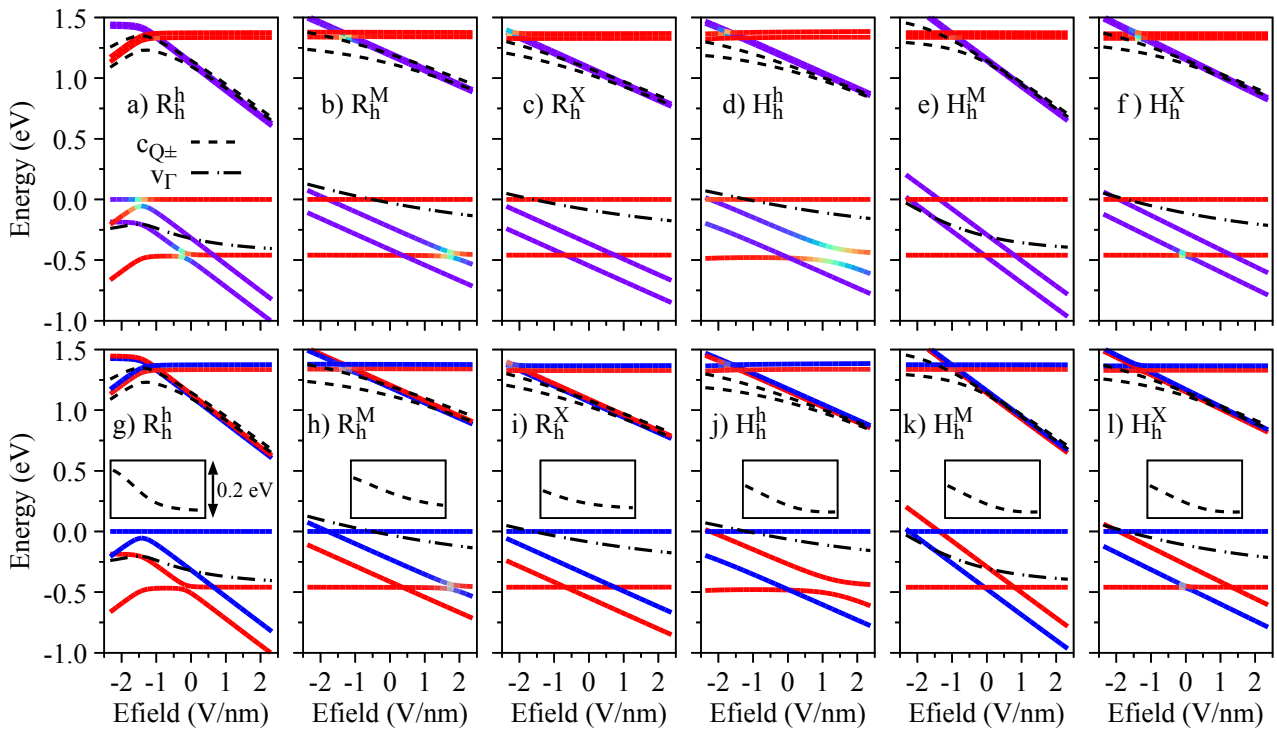


Figure 3. Energy dependence with respect to the electric field of the relevant low-energy bands (see Figure 1g) for all considered stackings: the top row, panels (a–f), indicates the color-coded layer decomposition of the K point bands (same color code as in Figures 1a–f); the bottom row, panels (g–l), indicates the color-coded spin decomposition of the K point bands (same color code as in Figures 2a–f); the insets in panels (g–l) show the energy difference between c_{Q+} and c_{Q-} bands, emphasizing an anti-crossing at larger electric fields.

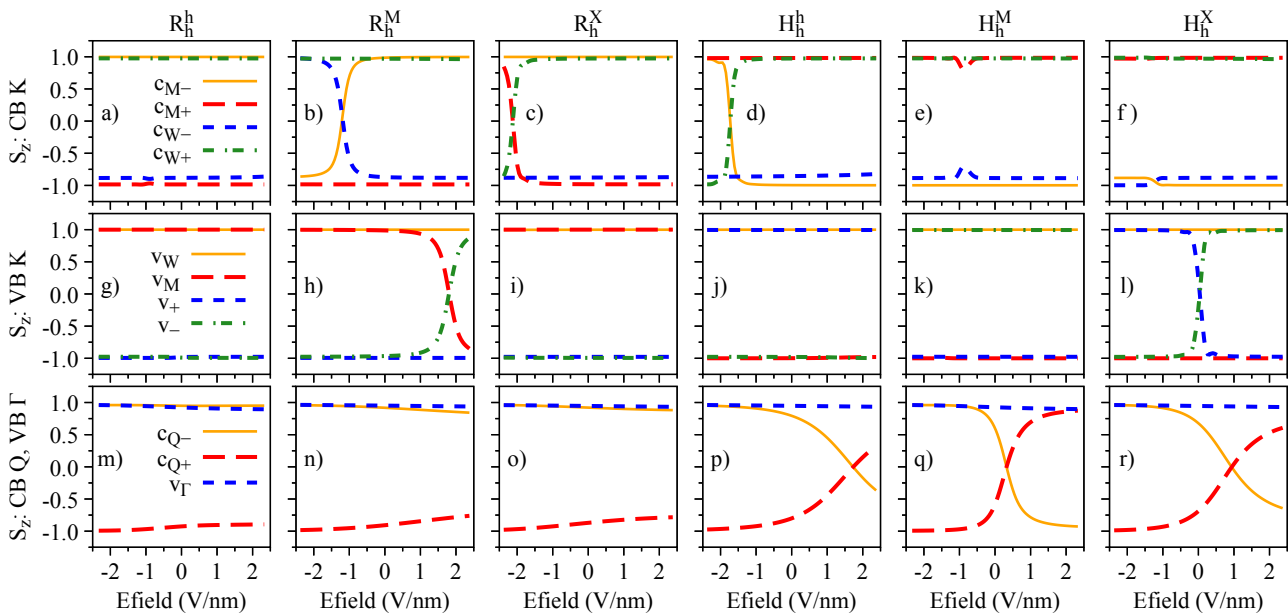


Figure 4. Spin degree of freedom, S_z , of the low-energy bands as a function of the applied electric field for the studied stackings R_h^h (a,g,m), R_h^M (b,h,n), R_h^X (c,i,o), H_h^h (d,j,p), H_h^M (e,k,q), and H_h^X (f,l,r).

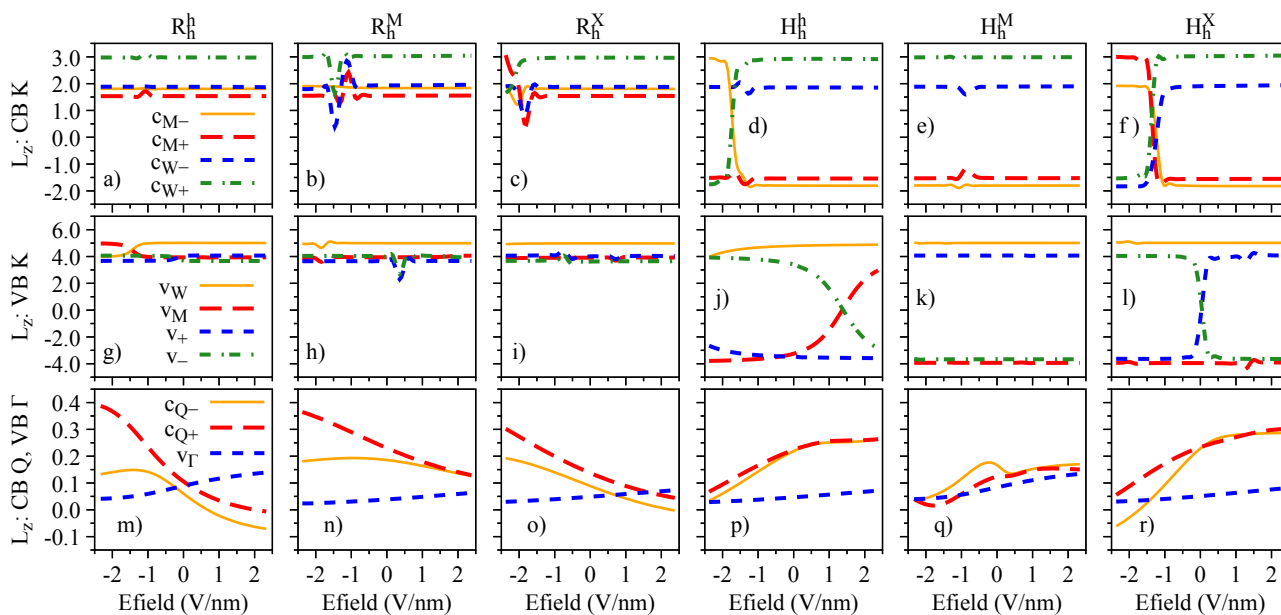


Figure 5. Same as Figure 4 but for the orbital degree of freedom, L_z .

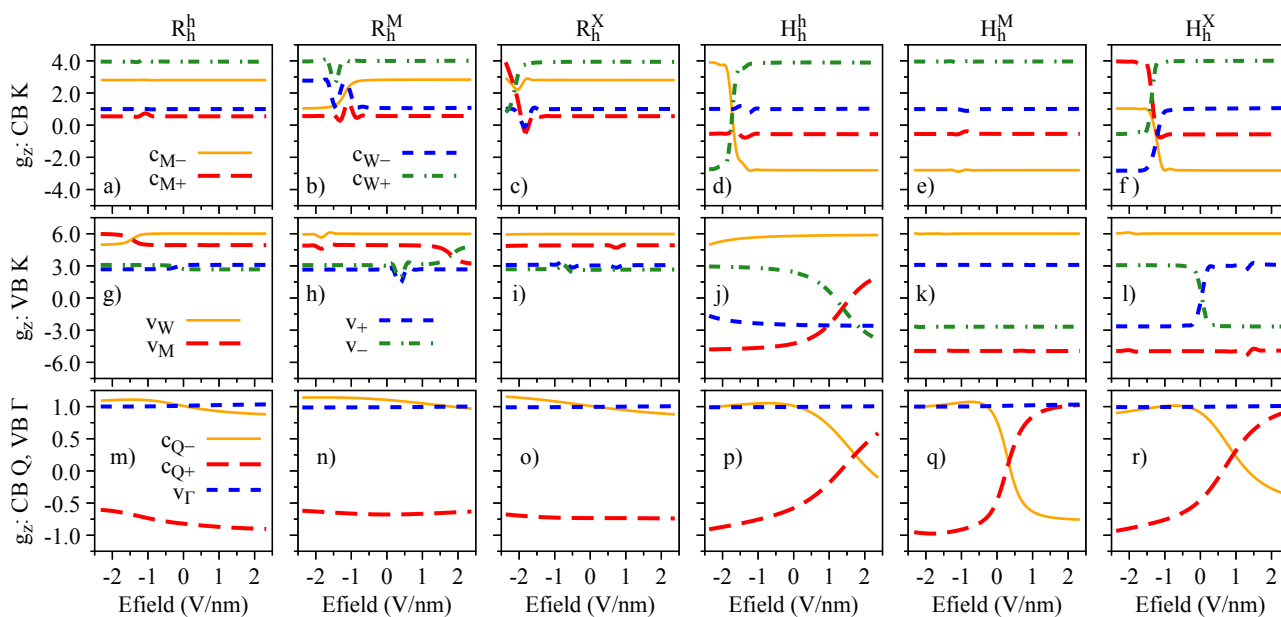


Figure 6. Same as Figures 4 and 5 but for the band g -factor, $g_z = L_z + S_z$.

3.3. Interlayer Distance Variation

In this section, we investigate the consequences of varying the equilibrium interlayer distance. This can be particularly relevant in the context of fluctuations introduced by the mechanical exfoliation and stamping procedures in TMDC heterostructures [47,56,63], which create regions with good and bad *interlayer contact*. Additionally, changes in the interlayer distance can provide insights into the effects of external out-of-plane pressure, which can be currently investigated in available experimental setups, such as the recently reported studies on graphene/WSe₂ [106], multilayered TMDCs [107], and WSe₂/Mo_{0.5}W_{0.5}Se₂ heterostructures [108]. On a more abstract and theoretical level, artificially varying the interlayer distance provides an additional knob with which to modify the interlayer hybridization [109] and analyze its impact on the spin and orbital angular momenta.

The influence of the interlayer distance variation on the energy levels, spin angular momenta, orbital angular momenta, and g -factors is presented in Figures 7, 8, 9, and 10, respectively. We restrict ourselves to fluctuations of $\pm 20\%$ of the equilibrium interlayer

distances given in Table 1. Overall, the same reasoning we discussed for the electric field effect applies to the interlayer distance variations. Nonetheless, we highlight a few points, to strengthen the discussions and understanding presented in the previous Section 3.2. There is a strong orbital mixing region visible in the lower valence bands with same spins in the R_h^h stacking case (Figure 7a,g), but with a negligible signature in the L_z (Figure 9g), as the monolayer values of L_z are all positive and close to each other. On the other hand, these hybridization effects are much stronger in the valence band of the H_h^X stacking case (Figure 7f,l), with strong signatures in the values of S_z and L_z (Figures 8l and 9l). We also note that in the H_h^h stacking, the most favorable for the 60° case, the g_z values of the valence band (particularly v_W) can be effectively altered by reducing the interlayer distance (also seen in the H_h^M stacking).

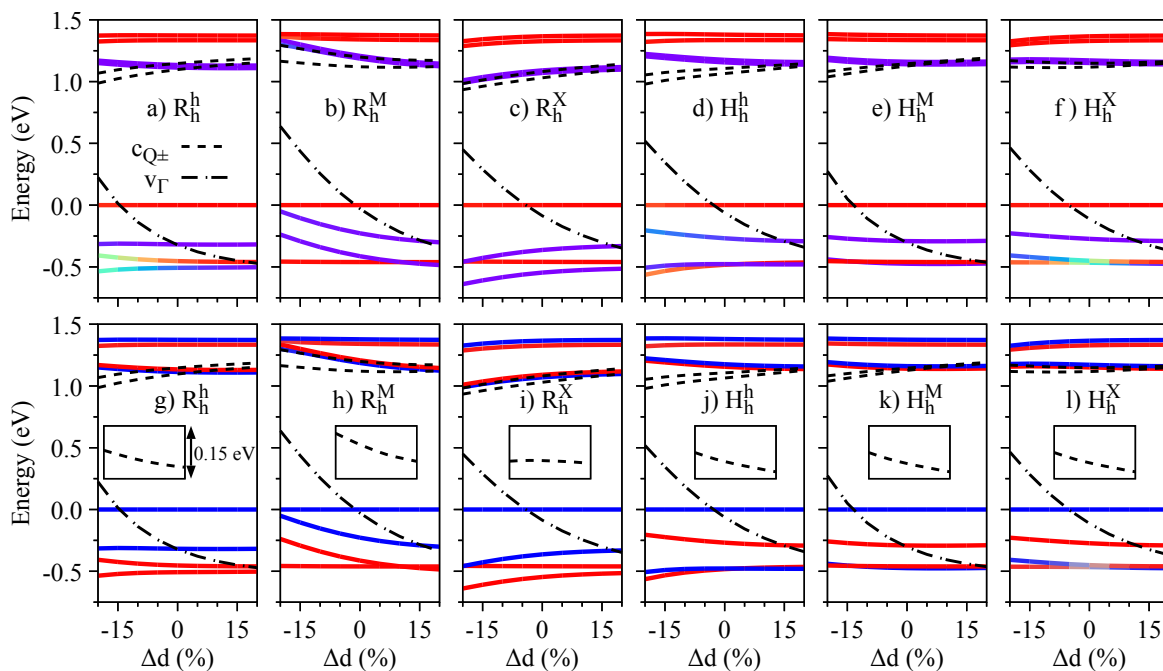


Figure 7. Same as Figure 3 but as a function of the interlayer distance variation.

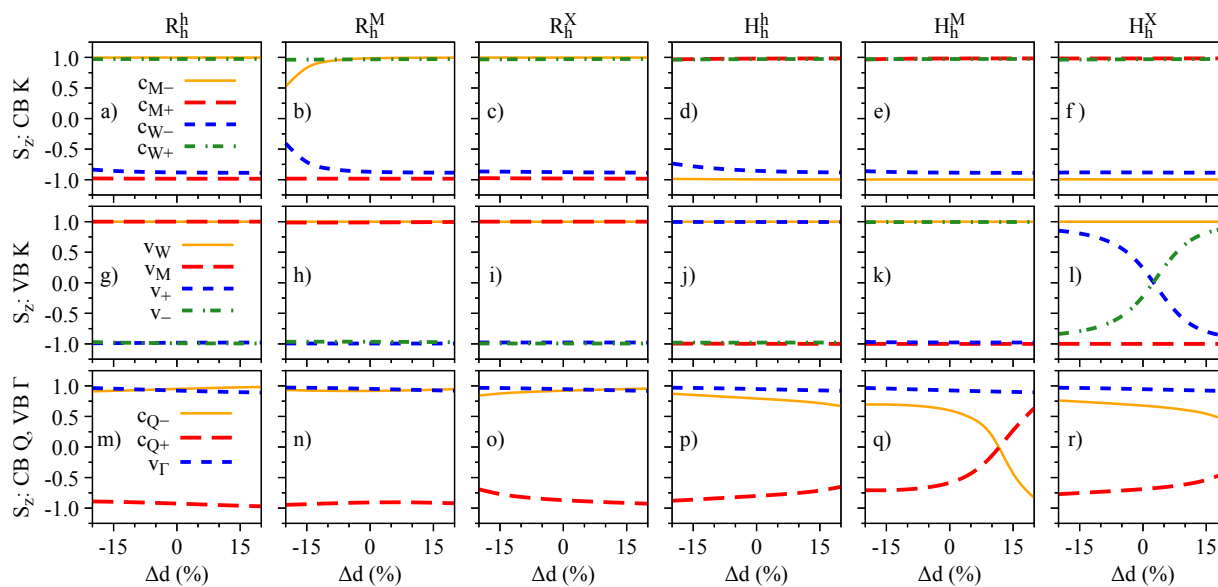


Figure 8. Same as Figure 4 but as a function of the interlayer distance variation.

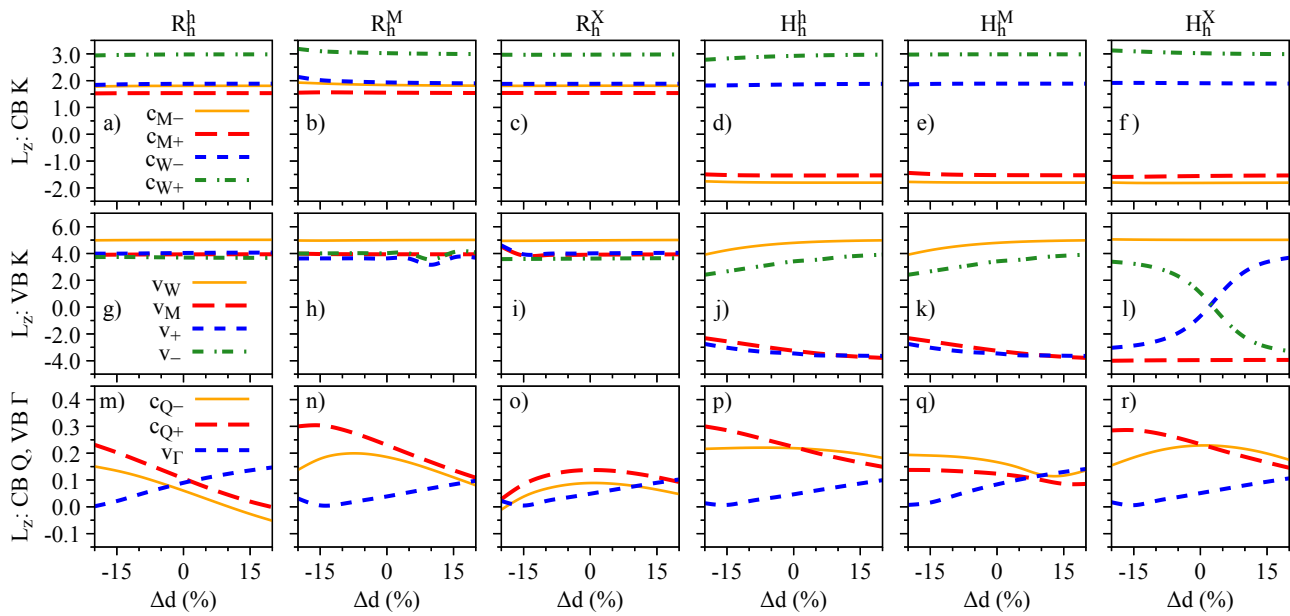


Figure 9. Same as Figure 5 but as a function of the interlayer distance variation.

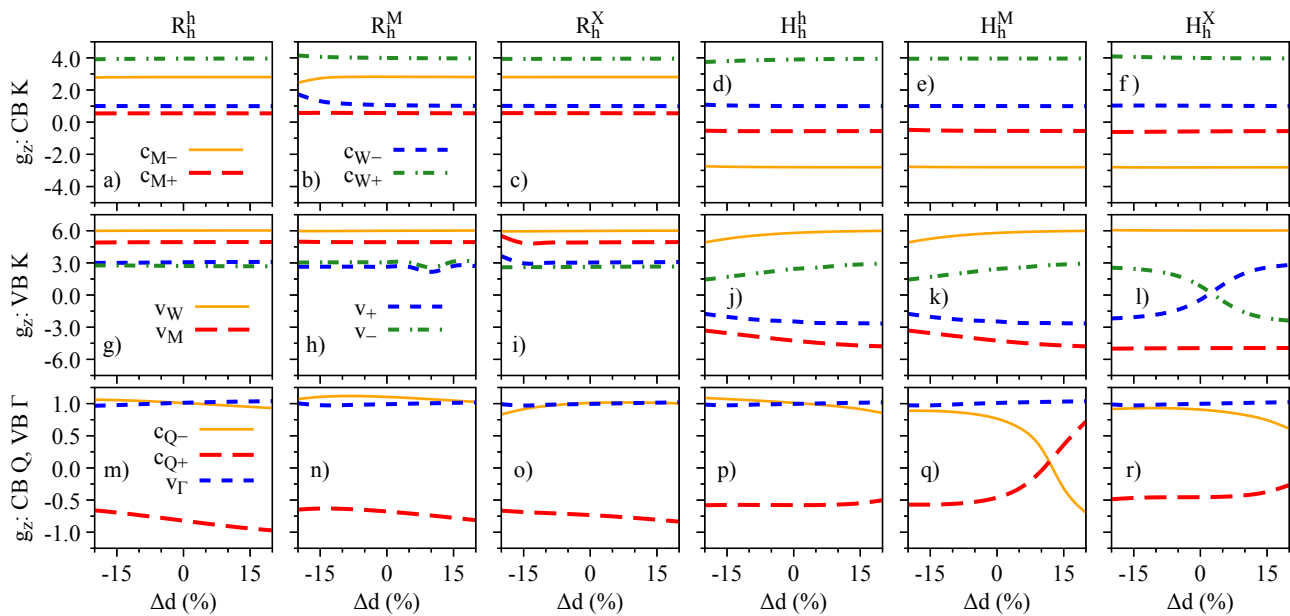


Figure 10. Same as Figure 6 but as a function of the interlayer distance variation.

4. Low-Energy Dipolar Excitons

In this section, we investigate the fundamental ingredients that characterize low-energy dipolar excitons: the electric dipole moment; polarizability; dipole matrix elements; and effective g-factors, based on the robust DFT calculations we presented in Sections 2 and 3. External factors that can alter the energetic landscape of such dipolar excitons, and consequently their photoluminescence or reflectance spectra, are beyond the scope of the present manuscript. Regarding the spin-valley physics and g-factors, previous studies focusing on intralayer excitons in monolayer TMDCs show that DFT calculations provide remarkable agreement with experimental data for pristine [110,111] and strained [85,94,95] cases. These intralayer excitons have larger conduction-to-valence band dipole matrix elements, larger electron-hole exchange contributions, and weaker dielectric screening, when compared to interlayer excitons. Therefore, if DFT is indeed capturing the relevant spin-valley properties of intralayer excitons, it will be sufficient to provide a reliable description of the spin-valley properties in dipolar excitons. In fact, DFT

studies on interlayer exciton g-factors [64,66,67] are indeed capable of providing reliable comparison with experiments.

4.1. Symmetry-Based Selection Rules

Starting from the symmetry perspective, we can use the irreps computed in Section 2 to characterize the optical selection rules of the possible interlayer excitons. Let us first discuss the selection rules of direct excitons at the K points, in order to compare with and validate our DFT calculations in the next Section, 4.3. Direct optical transitions are characterized by the matrix element mediated by the momentum operator:

$$\langle i|\vec{p} \cdot \hat{e}|f\rangle \sim \mathbb{I}_i^* \otimes \mathbb{I}_p \otimes \mathbb{I}_f, \tag{3}$$

in which $\mathbb{I}_{i(f)}$ is the irrep of the initial (final) state, and \mathbb{I}_p is the irrep of the momentum operator for a specific polarization ($\hat{e} = \{\sigma_+, \sigma_-, z\}$). The components of the momentum operator for circularly and linearly polarized light in the C_3 group transform as

$$K_1 \sim z, K_2 \sim \sigma_-, K_3 \sim \sigma_+. \tag{4}$$

Combining Equation (4) with the irreps of the valence and conduction bands given in Table 2, we can compute the optical selection rules for K-K dipolar excitons. The results are shown in Table 5, and agree with previous symmetry-based and DFT calculations [64,69,73]. It is also possible to verify that the *intralayer* optical selection rules are nicely preserved. For instance, transitions from $v_W(\mathbf{K})$ to $c_{W+}(\mathbf{K})$ provide σ_+ , whereas transitions from $v_M(\mathbf{K})$ to $c_{M-}(\mathbf{K})$ provide σ_+ for R-type stackings and σ_- for H-type stackings. An important point to discuss here is related to the so-called *spin-dark* optical transitions (sometimes also referred to as *spin-flip* or *spin-singlet* transitions): for instance, the $v_W(\mathbf{K}) \rightarrow c_{M-}(\mathbf{K})$ transition in the H_h^h stacking. The orientation of S_z , given in Tables 3 and 4, is not indicative of allowed or forbidden optical transitions: in fact, $S_z \neq 1$ if we increase the number digits after the decimal point in Tables 3 and 4. This is already evident in the monolayer case, due to the existence of the dark excitons [112–114]. The main point here is that SOC always introduces a mixing of spins (even in graphene [104]), and that the momentum matrix element does not flip spin (more discussions about spin-mixing and optical transitions for *spin-dark* states in monolayer TMDCs can be found in Ref. [95]). Furthermore, some of the interlayer optical transitions presented in Table 5 have the same structure as the dark/gray excitons in monolayers [112–114], i.e., one transition with z polarization and the other with σ_{\pm} . This feature actually explains the energy splitting of ~ 0.1 meV experimentally observed at zero magnetic field by Li and coauthors [51] in atomically reconstructed $MoSe_2/WSe_2$ heterobilayers, akin to the dark-gray exciton splitting of ~ 0.5 meV in pristine W-based monolayers [112,113].

Table 5. Symmetry-based selection rules for the direct interlayer excitons at the K point in the C_3 symmetry group.

	$v_W(\mathbf{K}) \rightarrow c_{M-}(\mathbf{K})$	$v_W(\mathbf{K}) \rightarrow c_{M+}(\mathbf{K})$
R_h^h	$K_4^* \otimes K_5 = K_3 \Rightarrow \sigma_+$	$K_4^* \otimes K_4 = K_1 \Rightarrow z$
R_h^M	$K_5^* \otimes K_5 = K_1 \Rightarrow z$	$K_5^* \otimes K_4 = K_2 \Rightarrow \sigma_-$
R_h^X	$K_6^* \otimes K_5 = K_2 \Rightarrow \sigma_-$	$K_6^* \otimes K_4 = K_3 \Rightarrow \sigma_+$
H_h^h	$K_6^* \otimes K_4 = K_3 \Rightarrow \sigma_+$	$K_6^* \otimes K_5 = K_2 \Rightarrow \sigma_-$
H_h^M	$K_5^* \otimes K_4 = K_2 \Rightarrow \sigma_-$	$K_5^* \otimes K_5 = K_1 \Rightarrow z$
H_h^X	$K_4^* \otimes K_4 = K_1 \Rightarrow z$	$K_4^* \otimes K_5 = K_3 \Rightarrow \sigma_+$

For optical transitions involving momentum-indirect dipolar excitons, i.e., transitions involving valence and conduction bands at different \vec{k} points, a phonon is required, to en-

sure momentum conservation. The optical transition matrix element mediated by phonons is written as [115]

$$\sum_l \langle i | H_{e-ph} | l \rangle (E_f - E_l)^{-1} \langle l | \vec{p} \cdot \hat{\epsilon} | f \rangle \sim \mathbb{I}_i^* \otimes \mathbb{I}_{ph} \otimes \mathbb{I}_p \otimes \mathbb{I}_f, \quad (5)$$

in which H_{e-ph} takes into account the electron-phonon coupling, and transforms as the irrep I_{ph} . It is beyond the scope of this manuscript to provide deeper insights into the strength of the electron-phonon coupling: rather, we discuss qualitatively the possible symmetry-allowed mechanisms involving the momentum-indirect dipolar excitons.

For indirect excitons with electrons and holes in opposite K valleys ($-K$ and K , sharing the same C_3 group), the direct product $\mathbb{I}_i^* \otimes \mathbb{I}_f$ provides the output shown in Table 6. Note that the output is always restricted to the irreps K_1 , K_2 , and K_3 . Phonons in the C_3 group would span all the irreps of the simple group, namely K_1 , K_2 , and K_3 . Combining the results given in Table 6, and performing a direct product with all possible phonon modes, we obtain

$$\begin{aligned} K_1 \otimes \{K_1, K_2, K_3\} &= \{K_1, K_2, K_3\} \\ K_2 \otimes \{K_1, K_2, K_3\} &= \{K_2, K_3, K_1\} \\ K_3 \otimes \{K_1, K_2, K_3\} &= \{K_3, K_1, K_2\} \end{aligned} \quad (6)$$

which always provides K_1 , K_2 , and K_3 . These irreps also encode the light polarization, as given in Equation (4). What our results suggest is that any type of phonon with momentum K can, in principle, mediate the optical recombination of dipolar excitons with electrons and holes residing in opposite K valleys. Perhaps some of these processes are not favored, due to off-resonant conditions and weak electron-phonon coupling, but could be effectively triggered when phonon energies are brought into resonance, such as was the case of the 24T anomaly [47,50,61]. Certainly, these phonon processes are intimately dependent on the strength of the electron-phonon couplings and how those couplings are translated for the final excitonic state (based on the particular conduction and valence bands constituents).

Table 6. Direct product of valence bands at the $-K$ point and conduction bands at the K point in the C_3 symmetry group.

	$v_W(-K) \rightarrow c_{M-}(K)$	$v_W(-K) \rightarrow c_{M+}(K)$
R_h^h	$K_5^* \otimes K_5 = K_1$	$K_5^* \otimes K_4 = K_2$
R_h^M	$K_4^* \otimes K_5 = K_3$	$K_4^* \otimes K_4 = K_1$
R_h^X	$K_6^* \otimes K_5 = K_2$	$K_6^* \otimes K_4 = K_3$
H_h^h	$K_6^* \otimes K_4 = K_3$	$K_6^* \otimes K_5 = K_2$
H_h^M	$K_4^* \otimes K_4 = K_1$	$K_4^* \otimes K_5 = K_3$
H_h^X	$K_5^* \otimes K_4 = K_2$	$K_5^* \otimes K_5 = K_1$

To investigate indirect dipolar excitons with holes at the Γ point and electrons at the K valley that do not have the same symmetry group, we must describe both conduction and valence band states on the same footing, using compatibility relations [89]. It is more convenient to go from a higher symmetry group to a lower symmetry group than the other way around. With this in mind, we mapped Γ point states to the K valley $\Gamma_4 \rightarrow K_4 \oplus K_5$ and present the direct product in Table 7. The same argument discussed in the case of electrons and holes at opposite valleys applies here, and multiple phonons with momentum K could trigger the optical recombination of such Γ - K excitons.

Finally, we discuss the indirect excitons involving conduction bands at the Q point and holes at either Γ or K points. As the C_1 symmetry group contains a single irrep in

the simple group, all electronic states, phonon modes, and operators are mapped onto this irrep: consequently, multiple phonon mediated processes are allowed. We note that Q–K transitions have been recently observed [45], supporting the idea that some of these symmetry-allowed phonons discussed here are indeed favoring the optical recombination.

Table 7. Direct product of valence bands at the Γ point and conduction bands at the K point in the C_3 symmetry group.

	R_h^h, R_h^M, R_h^X	H_h^h, H_h^M, H_h^X
$v_\Gamma(K_4) \rightarrow c_{M-}(K)$	$K_4^* \otimes K_5 = K_3$	$K_4^* \otimes K_4 = K_1$
$v_\Gamma(K_5) \rightarrow c_{M-}(K)$	$K_5^* \otimes K_5 = K_1$	$K_5^* \otimes K_4 = K_2$
$v_\Gamma(K_4) \rightarrow c_{M+}(K)$	$K_4^* \otimes K_4 = K_1$	$K_4^* \otimes K_5 = K_3$
$v_\Gamma(K_5) \rightarrow c_{M+}(K)$	$K_5^* \otimes K_4 = K_2$	$K_5^* \otimes K_5 = K_1$

4.2. Effective g-Factors

Combining the band g-factors studied in Section 3 with the optical selection rules discussed in Section 4.1, we investigate here the effective g-factors of the relevant dipolar excitons. As the momentum-indirect excitons require a phonon to mediate the optical emission, we can only determine unambiguously the sign of the g-factors for direct interlayer excitons, while for the other dipolar states we restrict ourselves to the magnitude of the g-factors. The dipolar exciton g-factors can be written as

$$g(X) = 2|g(c) \pm g(v)|, \quad (7)$$

in which $g(c)$ and $g(v)$ represent the conduction and valence band g-factors, and the \pm sign contemplates the two possibilities of time-reversal partners. For example, interlayer excitons with the valence band $v = v_W$ and the conduction bands $c = c_{M_0\pm}$ could be generated with v and c at the K point (direct in momentum), as indicated in Figure 1g, or with v in the K point and c in the $-K$ point (indirect in momentum).

The calculated g-factor values for the studied dipolar excitons are shown in Table 8. The largest absolute values stem from the KK dipolar excitons (v at K and c at K in H-type, v at $-K$ and c at K in R-type), as they involve the energy bands with the largest g-factors. Some dipolar excitons show very similar g-factors, such as the values related to $v_W(-K) \rightarrow c_{M+}(K)$ and $v_W(-K) \rightarrow c_{M+}(K)$ excitons in H-type stackings. We also observe g-factors with values < 1 , and even ~ 0 [$v_{\Gamma_1} \rightarrow c_{Q-}(Q)$], mainly originating from the valence bands at the Γ point. These different g-factors originate from different stackings, and distinct dipolar exciton species can be observed in the crossover region between deep and shallow moiré potentials, as a function of the twist angle or temperature; however, no systematic experimental study has been realized to explore such conditions. We emphasize that our calculated values are in excellent agreement with previously reported theoretical studies [57,64,67,80], and lie within the available experimental values, which range from -15 to -17 in H-type stackings [20,47–51,53,60,61], and from 5 to 8 in R-type stackings [20,42,48–51,116,117].

4.3. Electric Field Dependence

We now turn to the behavior of the different dipolar excitons as a function of the electric field. Motivated by the experimentally accessible regime [42–46], in which there is no indication of any crossings in the top valence band or lower conduction bands, we restrict ourselves to electric field values $\gtrsim -0.75$ V/nm, ensuring that the conduction band of MoSe₂ is always below the conduction band of WSe₂. For positive values of electric field, there are no visible band crossings, so we can extend our analysis towards electric field values of ~ 2 V/nm. In fact, some experimental studies that investigate dipolar excitons under electric field also show an asymmetric range [42,43,45], supporting the electric field values we consider here.

Table 8. Dipolar exciton g-factors involving the top valence band states (at Γ , K, and $-K$ points) to conduction bands of Mo at the K point ($c_{M\pm}$) or to the conduction bands at the Q point ($c_{Q\pm}$) at zero electric field and equilibrium interlayer distance. The g-factors with unambiguously determined signs are given in bold.

	R_h^h	R_h^M	R_h^X	H_h^h	H_h^M	H_h^X
$v_W(K) \rightarrow c_{M-}(K)$	-6.42	6.34	+6.34	-17.18	+17.62	17.66
$v_W(K) \rightarrow c_{M+}(K)$	10.93	+10.85	-10.84	+12.70	13.10	-13.18
$v_W(K) \rightarrow c_{Q-}(Q)$	10.01	9.78	9.94	9.56	10.49	10.22
$v_W(K) \rightarrow c_{Q+}(Q)$	13.67	13.34	13.42	12.74	12.94	12.94
$v_W(-K) \rightarrow c_{M-}(K)$	17.64	17.63	17.57	5.99	6.43	6.41
$v_W(-K) \rightarrow c_{M+}(K)$	13.13	13.12	13.07	10.47	10.94	10.89
$v_W(-K) \rightarrow c_{Q-}(Q)$	14.05	14.19	13.97	13.61	13.55	13.85
$v_W(-K) \rightarrow c_{Q+}(Q)$	10.39	10.63	10.49	10.43	11.10	11.12
$v_{\Gamma_1} \rightarrow c_{M-}(K)$	3.58	3.67	3.62	7.58	7.62	7.62
$v_{\Gamma_1} \rightarrow c_{M+}(K)$	0.92	0.85	0.87	3.10	3.10	3.14
$v_{\Gamma_1} \rightarrow c_{Q-}(Q)$	0.01	0.23	0.03	0.03	0.49	0.18
$v_{\Gamma_1} \rightarrow c_{Q+}(Q)$	3.66	3.33	3.46	3.14	2.94	2.90
$v_{\Gamma_2} \rightarrow c_{M-}(K)$	7.63	7.63	7.60	3.60	3.58	3.63
$v_{\Gamma_2} \rightarrow c_{M+}(K)$	3.13	3.12	3.11	0.88	0.94	0.85
$v_{\Gamma_2} \rightarrow c_{Q-}(Q)$	4.04	4.19	4.01	4.01	3.55	3.81
$v_{\Gamma_2} \rightarrow c_{Q+}(Q)$	0.39	0.63	0.52	0.83	1.10	1.08

The energy dependence of the dipolar excitons under external electric fields can be directly inferred from the dependence of the energy bands, because the effective mass is barely affected by the electric field (changes on the order of 10^{-3} – 10^{-2}), and the dielectric environment remains unchanged; therefore, the energy variation of the dipolar excitons with respect to the electric field can be extracted directly from the DFT calculations [63], and modeled by the following dependence [118,119]:

$$\Delta E(F_z) = -\mu F_z - \frac{\alpha}{2} F_z^2, \quad (8)$$

in which μ is the electric dipole moment (in meV nm/V), α is the polarizability (in meV nm²/V²), and F_z is the electric field in V/nm.

Our calculated values of the electric dipole moment and polarizabilities, fitted in the range of -0.7 to 0.7 V/nm, are presented in Figure 11. Overall, our results reveal that the values of μ (α) decrease (increase) as we go from momentum-direct to momentum-indirect dipolar excitons ($KK \rightarrow KQ \rightarrow \Gamma K \rightarrow \Gamma Q$), reflecting the degree of layer delocalization of the bands involved ($\Gamma > Q > K$, as shown in Figure 1a–f). These delocalization features have already been observed in the magnitude of interlayer excitons of WSe₂ homobilayer structures [120,121], and there is one report on MoSe₂/WSe₂ heterobilayers [45]. Our results also show that the spin-split conduction bands $c_{M\pm}$ have negligible effect on μ and α of KK and ΓK excitons, whereas the conduction bands $c_{Q\pm}$ provide different signatures, as they have different delocalization over the two layers. Particularly for the KK dipolar excitons, we note that the calculated values of α are quite small (0.2 – 2 meV nm²/V²), and that the two possible excitons stemming from $c_{M\pm}$ are nearly indistinguishable under the electric field dependence; however, they would have different emission energies (due to the SOC splitting of $c_{M\pm}$) and distinct g-factor signatures. We note that our calculated values of μ for KK and KQ dipolar excitons—and particularly that $\mu_{KK} > \mu_{KQ}$ —are consistent with recent GW + Bethe-Salpeter calculations and experiments in MoSe₂/WSe₂ heterobilayers [45].

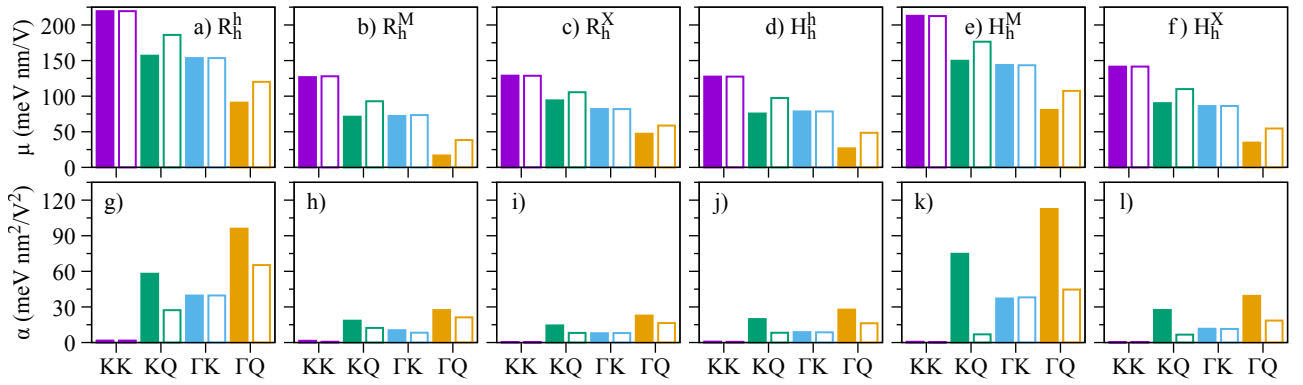


Figure 11. Calculated values of the electric dipole moments for (a) R_h^h , (b) R_h^M , (c) R_h^X , (d) H_h^h , (e) H_h^M , and (f) H_h^X stackings. Calculated values of the polarizabilities for (g) R_h^h , (h) R_h^M , (i) R_h^X , (j) H_h^h , (k) H_h^M , and (l) H_h^X stackings. The x-axis indicates the type of dipolar excitons (see Figure 1g). The values originating from $c_{M/Q-}$ ($c_{M/Q+}$) are shown with colored (open) boxes.

To validate the symmetry-based selection rules of the direct interlayer excitons discussed in Section 4.1, we present the dipole matrix elements computed within DFT in Figure 12. All the non-zero values match exactly the symmetry-based arguments discussed in Section 4.4. Generally, the dipole matrix elements decrease for increasing values of the electric field, with the exception of the p_{c_{M+},v_W} , which slightly increases for increasing electric field, reflecting the impact of the atomic registry on the wave functions of van der Waals heterostacks. Furthermore, the *spin-dark* optical transitions discussed in terms of symmetry in Section 4.1 are also present here. The momentum operator that enters the dipole matrix element (Equation (4)) does not flip spin, and therefore this transition is optically bright only if the 2-component spinors are mixed, which is indeed the case in our first-principles calculations with SOC. Our calculated values of the dipole matrix elements, along with their respective polarization, can be readily used to generate massive Dirac models for the dipolar excitons via the first-order perturbation within the \mathbf{k}, \mathbf{p} formalism, allowing the investigation of spin-dependent physics beyond the parabolic approximation [73,75].

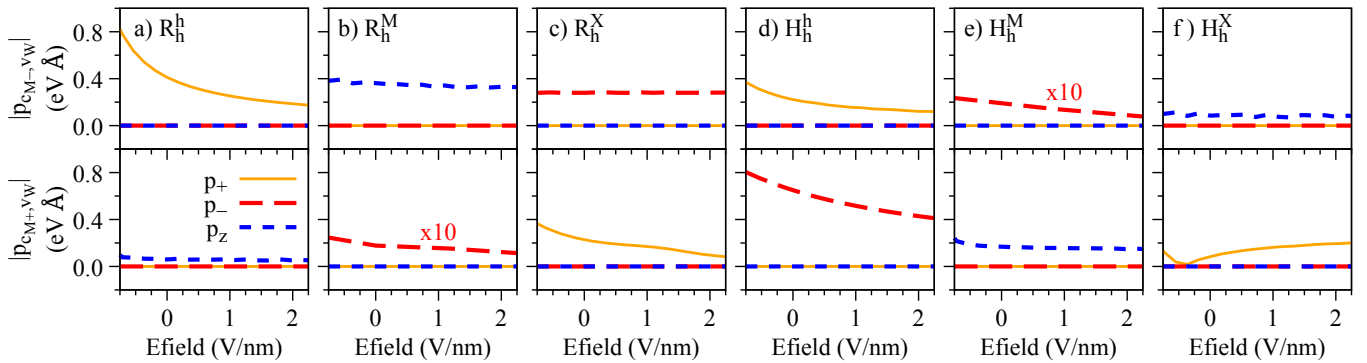


Figure 12. Absolute value of the dipole matrix element for interlayer transitions at the K point as a function of the electric field for (a) R_h^h , (b) R_h^M , (c) R_h^X , (d) H_h^h , (e) H_h^M , and (f) H_h^X stackings.

Based on the calculated values of the energy dependence and dipole matrix elements, with respect to the electric field, we can evaluate the radiative lifetime for direct dipolar excitons, given by [122,123]:

$$\tau_{\text{rad}} = \frac{\sqrt{\varepsilon_b} c \hbar^2}{2\pi e^2} \frac{E_0}{|p_{c,v}|^2 |\phi(0)|^2}, \quad (9)$$

with ε_b being the high-frequency dielectric constant of the environment, c the speed of light, \hbar the reduced Planck constant, e the electron charge, E_0 the exciton energy, and $|\phi(0)|^2$

the exciton envelope function evaluated at the origin. The relevant quantities that depend on the electric field, F_z , are the exciton energy, $E_0 \rightarrow E_0 + \Delta E(F_z)$ (see Equation (1)), and the dipole matrix element, $p_{c,v} \rightarrow p_{c,v}(F_z)$ (see Figure 12). Typical interlayer excitons exhibit lifetimes reaching almost 100 ns at very low temperatures, and a few ns at room temperature [39–41], with roughly one order of magnitude fluctuation when comparing different samples. To understand the isolated impact of the electric field on the radiative lifetime of the direct dipolar excitons, we consider the quantity

$$\frac{\tau_{\text{rad}}(F_z)}{\tau_{\text{rad}}(0)} = \frac{E_0 + \Delta E(F_z)}{E_0} \frac{|p_{c,v}(0)|^2}{|p_{c,v}(F_z)|^2}, \quad (10)$$

and display its calculated values in Figure 13 as a function of the electric field. The calculated ratio $\tau_{\text{rad}}(F_z)/\tau_{\text{rad}}(0)$ varies in general in a range from 0.5 to 4.5, except in the case of H_h^X , which shows a drastic increase in the radiative lifetime, because the dipole matrix element decreases to nearly zero in Figure 12f. Particularly for the high-symmetry stacking H_h^h , which is the most favorable one for $\sim 60^\circ$ samples, both direct dipolar excitons (singlet and triplet) exhibit an increase in the radiative lifetime as the electric field increases, which can be accessed experimentally in current devices.

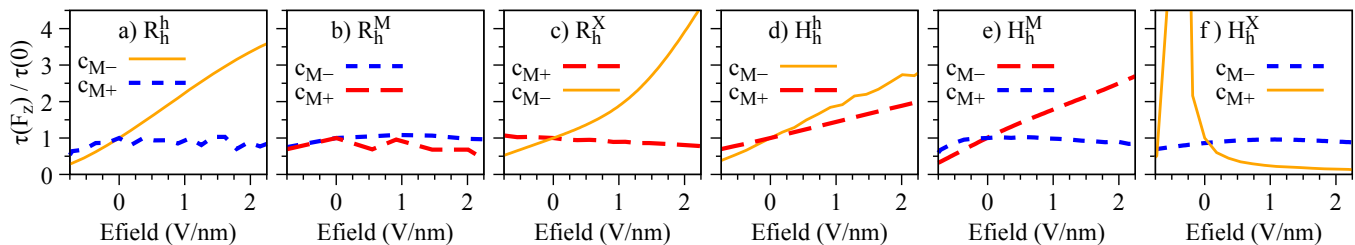


Figure 13. Calculated ratio $\tau_{\text{rad}}(F_z)/\tau_{\text{rad}}(0)$ as a function of the electric field for (a) R_h^h , (b) R_h^M , (c) R_h^X , (d) H_h^h , (e) H_h^M , and (f) H_h^X stackings. We use $E_0 = 1.35$ eV for all cases, and the calculated values of μ given in Figure 11. The contribution of α is neglected, as they nearly vanish for KK dipolar excitons.

Let us now discuss electric field effects on the valley Zeeman physics of the dipolar excitons (schematically shown in Figure 1g). The effective g-factors calculated via Equation (7) as a function of the electric field are shown in Figure 14 for all the considered R- and H-type stackings. Our results reveal that these dipolar excitons have a very robust valley Zeeman, barely changing under external electric field. The only exceptions are the dipolar excitons involving Q bands in the H-type stackings. Because of the g-factor crossing between the c_{Q+} and c_{Q-} bands (see Figure 6p,q,r), stemming from the spin mixing effects (see Figures 4p,q,r and 5p,q,r), the valley Zeeman of these indirect dipolar excitons is affected, and exhibits pronounced changes for increasing electric fields (see Figure 14d–f,j–l,p–r,v,x,y). Therefore, without significant band hybridization, the dipolar excitons retain their valley Zeeman signatures over a large range of applied electric field values, which can be particularly relevant for electrically-driven opto-spintronics applications [17]. In fact, our results reveal very fundamental and general features about the valley Zeeman mixing of excitonic states (including dipolar excitons) in 2D materials and van der Waals heterostructures—in this case, stemming from the band hybridization between different layers. Clear signatures of the valley Zeeman mixing on the excitonic states are still rather limited, but have been already observed experimentally in a few systems: strained WS_2 monolayers [85]; defect-mediated excitons in MoS_2 monolayers [97,98]; WS_2 /graphene heterostructures [27]; and electrically-controlled trilayer $MoSe_2$ structures [124].

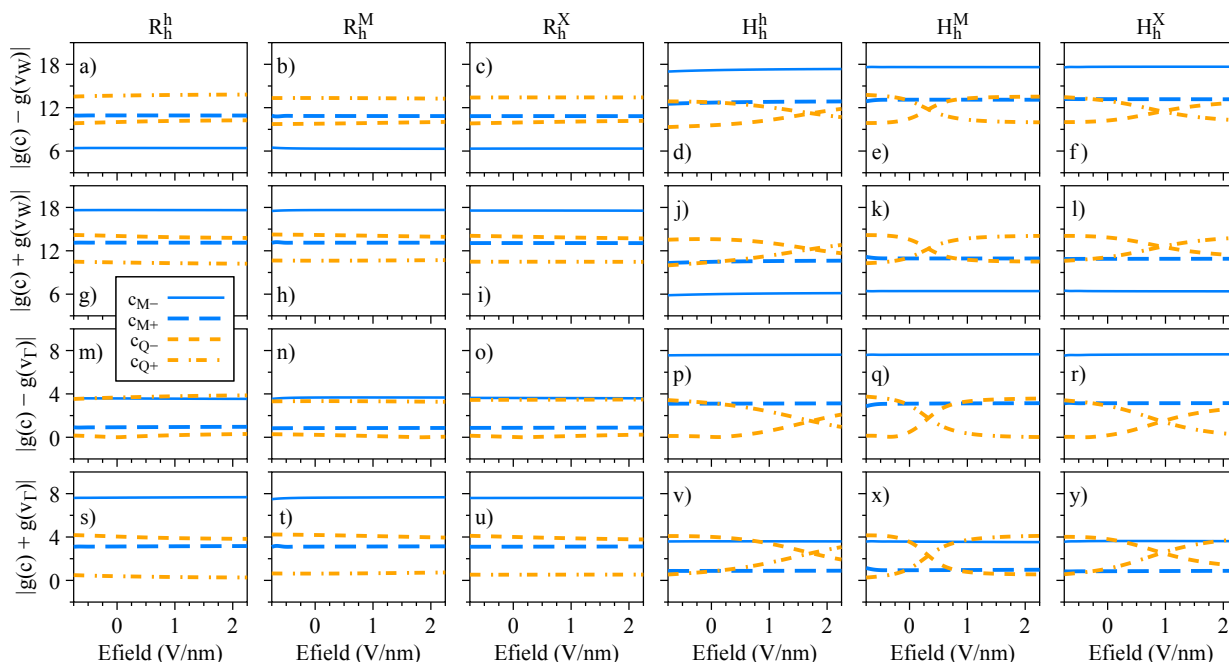


Figure 14. Dipolar exciton g-factors as a function of the electric field for the R- and H-type systems studied for the cases (a–f) $|g(c) - g(v_W)|$, (g–l) $|g(c) + g(v_W)|$, (m–r) $|g(c) - g(v_T)|$ and (s–v,x,y) $|g(c) + g(v_T)|$.

4.4. Interlayer Distance Variation

In this section, we focus on the effect of the interlayer distance variation. Our calculated values of the dipole matrix elements and the g-factors are presented in Figure 15 and Figure 16, respectively, and follow the same convention as discussed in the case of the electric field (Figures 12 and 14). In particular, we find a strong decrease of the dipole matrix elements as the interlayer distance increases, consequently making the dipolar excitons less optically active. These findings provide support to the idea that weakly coupled heterobilayers (with an interlayer separation larger than the equilibrium distance)—with, perhaps, additional electric field displacements due to asymmetric bottom and top environments—may exhibit highly quenched optical emission of dipolar excitons [56,63]; furthermore, as the dipole matrix elements behave in a fashion similar to the electric field, we expect similar behavior for the quantity $\tau_{\text{rad}}(F_z)/\tau_{\text{rad}}(0)$. Another interesting aspect, visible in the H_h^h stacking, is the decrease of the valley Zeeman originating from the top valence band at the K point, v_W , as the interlayer distance decreases (Figure 16d,j): we believe that this feature could be experimentally probed, using external pressure [106,107], which would effectively decrease the interlayer distance. For the H_h^M stacking, we also observe the signatures of Q-band mixing and reversal of the g-factor values as the interlayer distance increases.

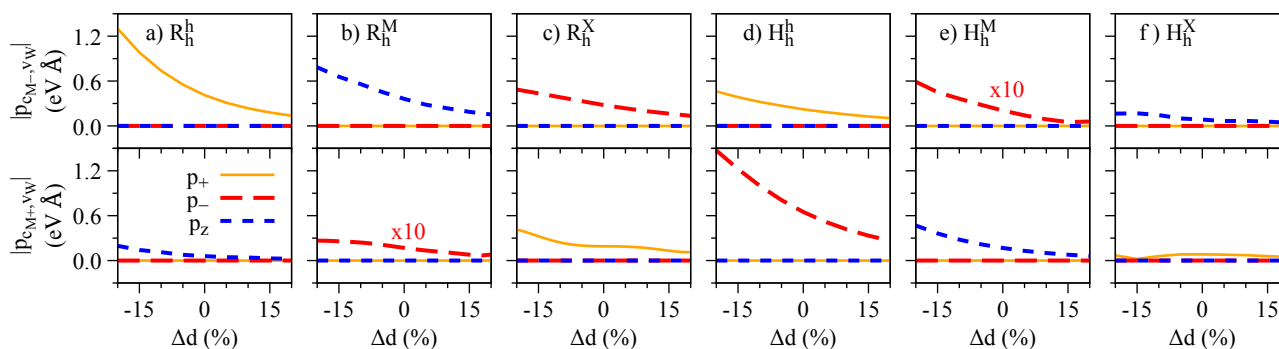


Figure 15. Same as Figure 12 but as a function of the interlayer distance.

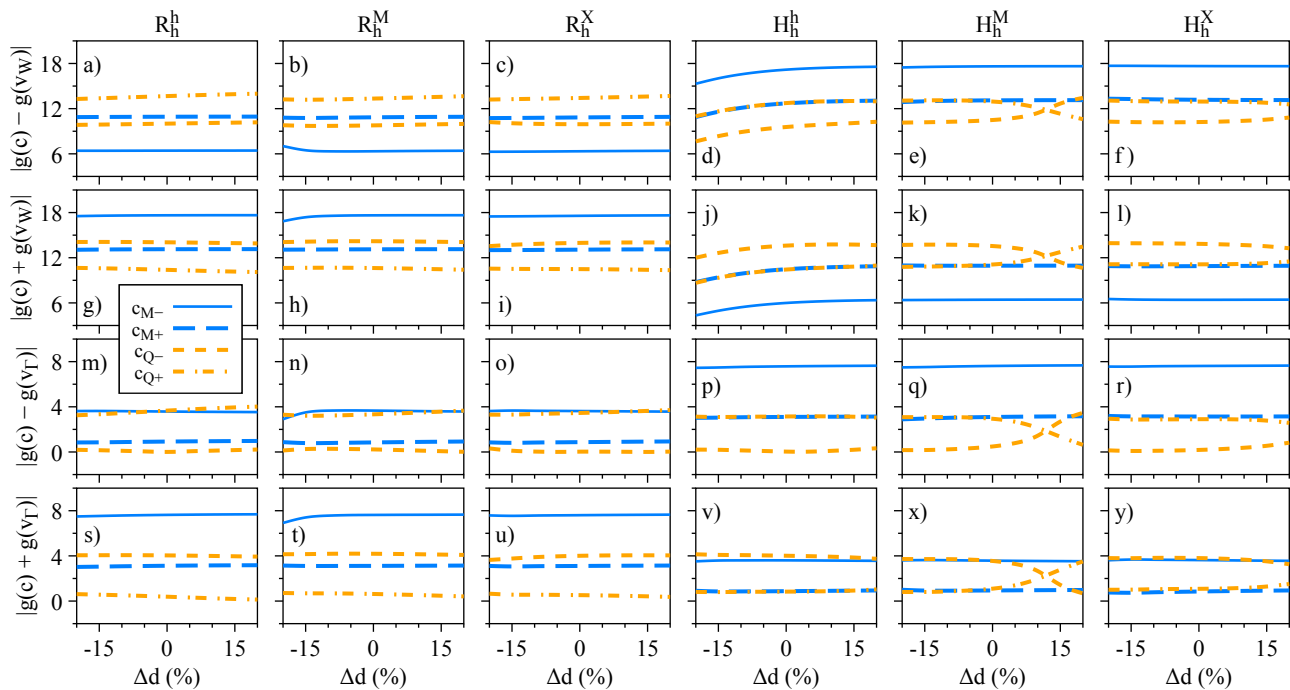


Figure 16. Same as Figure 14 but as a function of the interlayer distance.

5. Concluding Remarks

In summary, we have performed detailed first-principles calculations on the spin-valley physics of MoSe₂/WSe₂ heterobilayers under the effect of out-of-plane electric fields and as a function of the interlayer separation. Specifically, we have investigated the spin and orbital degrees of freedom, g-factors, and symmetry properties of the relevant band edges (located at the K, Q and Γ points) of high-symmetry stackings with 0° (R-type) and 60° (H-type) twist angles. These R- and H-type stackings are the fundamental building blocks present in moiré and atomically reconstructed supercells, experimentally observed in samples with small twist angles. Our calculations reveal distinct hybridization signatures of the spin and orbital degrees of freedom as a function of the electric field and interlayer separation, depending on the energy band and on the stacking configuration. With this crucial knowledge of the spin-valley physics of the band edges, we expanded our analysis to the low-energy dipolar (interlayer) excitons, either direct or indirect in k -space. We found that these different dipolar exciton species present distinct electric dipole moments, polarizabilities, and valley Zeeman signatures (g-factors), due to the particular mixing of the spin and orbital angular momenta from their constituent energy bands. We also performed a symmetry analysis to discuss the phonon modes that could mediate the optical recombination of momentum-indirect dipolar excitons. Regarding the valley Zeeman signatures of the interlayer excitonic states, our calculations revealed that direct dipolar excitons at the K-valley carry a robust valley Zeeman effect nearly independent of the electric field. On the other hand, the momentum-indirect dipolar excitons in the H-type stackings, with valence band at the K valleys and conduction bands at the Q valleys, showed a pronounced dependence of the valley Zeeman for positive values on applied electric fields. This peculiar g-factor dependence was unambiguously related to the spin-mixing of conduction bands at the Q point, which was absent in the R-type stackings. The valley Zeeman physics of the investigated dipolar excitons could also be affected by varying the interlayer distance, which could be experimentally probed under external pressure. As in the case of external electric fields, the interlayer variation effects in the valley Zeeman signatures were more pronounced in H-type stackings, and were more likely to be observed in samples with twist angle close to 60°.

Although *intralayer* excitons were not within the scope of the present manuscript, these quasiparticles are still optically active and easily recognized in the photoluminescence or

reflectivity spectra of MoSe₂/WSe₂ heterobilayers [39,47,99]. In particular, our g-factor calculations for the band edges (Figure 6) suggest that *intralayer* excitons could also provide valuable information on the interlayer hybridization via the valley Zeeman as a function of the electric field. Gated devices based on MoSe₂/WSe₂ heterostructures are within experimental reach [18,42,46], and could be used to test our hypothesis. We note that, in order to properly evaluate the *intralayer* exciton physics, it would be desirable to go beyond DFT calculations, and to employ the GW + Bethe–Salpeter formalism [45,65,97,125], which is beyond the scope of this work. Nonetheless, as these *intralayer* excitons are also quite localized in *k*-space [10,14,27], the spin and orbital angular momenta of the Bloch bands should account for the majority of the hybridization effects.

We emphasize that the theoretical approach employed here in our study is robust, and provides quantitative microscopic insights into the spin-valley physics of these van der Waals heterobilayers. This framework can certainly be extended to more complex multilayered van der Waals heterostructures that also host dipolar excitons: for instance, large-angle twisted MoSe₂/WSe₂ [126,127], homobilayers [22,125], trilayer hetero- and homo-structures [124,128,129], and MoSe₂/WS₂ heterobilayers [99,130,131].

Author Contributions: Conceptualization, P.E.F.J. and J.F.; methodology, P.E.F.J.; software, P.E.F.J.; validation, P.E.F.J.; formal analysis, P.E.F.J.; investigation, P.E.F.J.; resources, P.E.F.J.; data curation, P.E.F.J.; writing—original draft preparation, P.E.F.J. and J.F.; writing—review and editing, P.E.F.J. and J.F.; visualization, P.E.F.J. and J.F.; supervision, J.F.; project administration, P.E.F.J. and J.F.; funding acquisition, J.F. All authors have read and agreed to the published version of the manuscript.

Funding: The authors acknowledge the financial support of the Deutsche Forschungsgemeinschaft (DFG, German Research Foundation) SFB 1277 (Project-ID 314695032, projects B07 and B11), SPP 2244 (Project No. 443416183), and of the European Union Horizon 2020 Research and Innovation Program under Contract No. 881603 (Graphene Flagship).

Data Availability Statement: Not applicable.

Acknowledgments: We thank Yaroslav Zhumagulov and Christian Schüller for helpful discussions, and Sivan Refaely-Abramson for valuable insights into interlayer excitons.

Conflicts of Interest: The authors declare no conflict of interest.

Appendix A. Computational Details

The DFT were performed using the WIEN2k code [81], which implements a full potential all-electron scheme with augmented plane wave plus local orbitals (APW+lo) method. The crystal structures of monolayers and the heterostructure were generated using the atomic simulation environment (ASE) python package [132]. We used the Perdew–Burke–Ernzerhof exchange–correlation functional [133], a Monkhorst–Pack *k*-grid of 15 × 15, and self-consistent convergence criteria of 10^{−6} e for the charge and 10^{−6} Ry for the energy. For the heterostructures, van der Waals corrections [134] were taken into account in the self-consistent cycle. The core–valence energy separation was chosen as −6 Ry, the atomic spheres were expanded in orbital quantum numbers up to 10, and the plane wave cut-off multiplied by the smallest atomic radii was set to 9. For the inclusion of SOC, core electrons were considered fully relativistically, whereas valence electrons were treated in a second variational step [135], with the scalar-relativistic wave functions calculated in an energy window of −10 to 8 Ry. This upper energy limit provided a sufficiently large number of bands (~1500) to guarantee the proper convergence of the orbital angular momentum, as shown in Refs. [64,66,95]. The applied out-of-plane electric field was included as a zig-zag potential added to the exchange–correlation functional [136] with 40 Fourier coefficients. The structural parameters are discussed in Section 2.

References

1. Mak, K.F.; Lee, C.; Hone, J.; Shan, J.; Heinz, T.F. Atomically Thin MoS₂: A New Direct-Gap Semiconductor. *Phys. Rev. Lett.* **2010**, *105*, 136805. [[CrossRef](#)] [[PubMed](#)]
2. Splendiani, A.; Sun, L.; Zhang, Y.; Li, T.; Kim, J.; Chim, C.Y.; Galli, G.; Wang, F. Emerging photoluminescence in monolayer MoS₂. *Nano Lett.* **2010**, *10*, 1271. [[CrossRef](#)] [[PubMed](#)]
3. Kuc, A.; Zibouche, N.; Heine, T. Influence of quantum confinement on the electronic structure of the transition metal sulfide TS₂. *Phys. Rev. B* **2011**, *83*, 245213. [[CrossRef](#)]
4. Kumar, A.; Ahluwalia, P. Electronic structure of transition metal dichalcogenides monolayers 1H-MX₂ (M = Mo, W; X = S, Se, Te) from ab-initio theory: New direct band gap semiconductors. *Eur. Phys. J. B* **2012**, *85*, 186. [[CrossRef](#)]
5. Xiao, D.; Liu, G.B.; Feng, W.; Xu, X.; Yao, W. Coupled Spin and Valley Physics in Monolayers of MoS₂ and Other Group-VI Dichalcogenides. *Phys. Rev. Lett.* **2012**, *108*, 196802. [[CrossRef](#)]
6. Mak, K.F.; He, K.; Shan, J.; Heinz, T.F. Control of valley polarization in monolayer MoS₂ by optical helicity. *Nat. Nanotechnol.* **2012**, *7*, 494. [[CrossRef](#)]
7. Mak, K.F.; McGill, K.L.; Park, J.; McEuen, P.L. The valley Hall effect in MoS₂ transistors. *Science* **2014**, *344*, 1489. [[CrossRef](#)]
8. Qiu, D.Y.; da Jornada, F.H.; Louie, S.G. Optical Spectrum of MoS₂: Many-Body Effects and Diversity of Exciton States. *Phys. Rev. Lett.* **2013**, *111*, 216805. [[CrossRef](#)]
9. Xu, X.; Yao, W.; Xiao, D.; Heinz, T.F. Spin and pseudospins in layered transition metal dichalcogenides. *Nat. Phys.* **2014**, *10*, 343. [[CrossRef](#)]
10. Chernikov, A.; Berkelbach, T.C.; Hill, H.M.; Rigosi, A.; Li, Y.; Aslan, O.B.; Reichman, D.R.; Hybertsen, M.S.; Heinz, T.F. Exciton Binding Energy and Nonhydrogenic Rydberg Series in Monolayer WS₂. *Phys. Rev. Lett.* **2014**, *113*, 076802. [[CrossRef](#)]
11. Stier, A.V.; McCreary, K.M.; Jonker, B.T.; Kono, J.; Crooker, S.A. Exciton diamagnetic shifts and valley Zeeman effects in monolayer WS₂ and MoS₂ to 65 Tesla. *Nat. Commun.* **2016**, *7*, 10643. [[CrossRef](#)]
12. Schaibley, J.R.; Yu, H.; Clark, G.; Rivera, P.; Ross, J.S.; Seyler, K.L.; Yao, W.; Xu, X. Valleytronics in 2D materials. *Nat. Rev. Mater.* **2016**, *1*, 16055. [[CrossRef](#)]
13. Raja, A.; Chaves, A.; Yu, J.; Arefe, G.; Hill, H.M.; Rigosi, A.F.; Berkelbach, T.C.; Nagler, P.; Schüller, C.; Korn, T.; et al. Coulomb engineering of the bandgap and excitons in two-dimensional materials. *Nat. Commun.* **2017**, *8*, 15251. [[CrossRef](#)] [[PubMed](#)]
14. Wang, G.; Chernikov, A.; Glazov, M.M.; Heinz, T.F.; Marie, X.; Amand, T.; Urbaszek, B. Colloquium: Excitons in atomically thin transition metal dichalcogenides. *Rev. Mod. Phys.* **2018**, *90*, 021001. [[CrossRef](#)]
15. Geim, A.K.; Grigorieva, I.V. Van der Waals heterostructures. *Nature* **2013**, *499*, 419. [[CrossRef](#)]
16. Song, J.C.W.; Gabor, N.M. Electron quantum metamaterials in van der Waals heterostructures. *Nat. Nanotechnol.* **2018**, *13*, 986. [[CrossRef](#)]
17. Sierra, J.F.; Fabian, J.; Kawakami, R.K.; Roche, S.; Valenzuela, S.O. Van der Waals heterostructures for spintronics and optospintronics. *Nat. Nanotechnol.* **2021**, *16*, 856. [[CrossRef](#)]
18. Ciarrocchi, A.; Tagarelli, F.; Avsar, A.; Kis, A. Excitonic devices with van der Waals heterostructures: Valleytronics meets twistrionics. *Nat. Rev. Mater.* **2022**, *7*, 449. [[CrossRef](#)]
19. Tran, K.; Moody, G.; Wu, F.; Lu, X.; Choi, J.; Kim, K.; Rai, A.; Sanchez, D.A.; Quan, J.; Singh, A.; et al. Evidence for moiré excitons in van der Waals heterostructures. *Nature* **2019**, *567*, 71. [[CrossRef](#)] [[PubMed](#)]
20. Seyler, K.L.; Rivera, P.; Yu, H.; Wilson, N.P.; Ray, E.L.; Mandrus, D.G.; Yan, J.; Yao, W.; Xu, X. Signatures of moiré-trapped valley excitons in MoSe₂/WSe₂ heterobilayers. *Nature* **2019**, *567*, 66. [[CrossRef](#)]
21. Leisgang, N.; Shree, S.; Paradisanos, I.; Sponfeldner, L.; Robert, C.; Lagarde, D.; Balocchi, A.; Watanabe, K.; Taniguchi, T.; Marie, X.; et al. Giant Stark splitting of an exciton in bilayer MoS₂. *Nat. Nanotechnol.* **2020**, *15*, 901. [[CrossRef](#)] [[PubMed](#)]
22. Lin, K.Q.; Faria Junior, P.E.; Bauer, J.M.; Peng, B.; Monserrat, B.; Gmitra, M.; Fabian, J.; Bange, S.; Lupton, J.M. Twist-angle engineering of excitonic quantum interference and optical nonlinearities in stacked 2D semiconductors. *Nat. Commun.* **2021**, *12*, 1553. [[CrossRef](#)]
23. Gmitra, M.; Fabian, J. Graphene on transition-metal dichalcogenides: A platform for proximity spin-orbit physics and optospintronics. *Phys. Rev. B* **2015**, *92*, 155403. [[CrossRef](#)]
24. Gmitra, M.; Kochan, D.; Högl, P.; Fabian, J. Trivial and inverted Dirac bands and the emergence of quantum spin Hall states in graphene on transition-metal dichalcogenides. *Phys. Rev. B* **2016**, *93*, 155104. [[CrossRef](#)]
25. Avsar, A.; Unuchek, D.; Liu, J.; Sanchez, O.L.; Watanabe, K.; Taniguchi, T.; Özyilmaz, B.; Kis, A. Optospintronics in Graphene via Proximity Coupling. *ACS Nano* **2017**, *11*, 11678. [[CrossRef](#)] [[PubMed](#)]
26. Luo, Y.K.; Xu, J.; Zhu, T.; Wu, G.; McCormick, E.J.; Zhan, W.; Neupane, M.R.; Kawakami, R.K. Opto-Valleytronic Spin Injection in Monolayer MoS₂/Few-Layer Graphene Hybrid Spin Valves. *Nano Lett.* **2017**, *17*, 3877. [[CrossRef](#)]
27. Faria Junior, P.E.; Naimer, T.; McCreary, K.M.; Jonker, B.T.; Finley, J.J.; Crooker, S.; Fabian, J.; Stier, A.V. Proximity-enhanced valley Zeeman splitting at the WS₂/graphene interface. *arXiv* **2023**, arXiv:2301.12234.
28. Cadiz, F.; Courtade, E.; Robert, C.; Wang, G.; Shen, Y.; Cai, H.; Taniguchi, T.; Watanabe, K.; Carrere, H.; Lagarde, D.; et al. Excitonic Linewidth Approaching the Homogeneous Limit in MoS₂-Based van der Waals Heterostructures. *Phys. Rev. X* **2017**, *7*, 021026. [[CrossRef](#)]

29. Goryca, M.; Li, J.; Stier, A.V.; Taniguchi, T.; Watanabe, K.; Courtade, E.; Shree, S.; Robert, C.; Urbaszek, B.; Marie, X.; et al. Revealing exciton masses and dielectric properties of monolayer semiconductors with high magnetic fields. *Nat. Commun.* **2019**, *10*, 4172. [[CrossRef](#)]
30. Yankowitz, M.; Ma, Q.; Jarillo-Herrero, P.; LeRoy, B.J. van der Waals heterostructures combining graphene and hexagonal boron nitride. *Nat. Rev. Phys.* **2019**, *1*, 112. [[CrossRef](#)]
31. Zollner, K.; Faria Junior, P.E.; Fabian, J. Proximity exchange effects in MoSe₂ and WSe₂ heterostructures with CrI₃: Twist angle, layer, and gate dependence. *Phys. Rev. B* **2019**, *100*, 085128. [[CrossRef](#)]
32. Zollner, K.; Faria Junior, P.E.; Fabian, J. Strong manipulation of the valley splitting upon twisting and gating in MoSe₂/CrI₃ and WSe₂/CrI₃ van der Waals heterostructures. *Phys. Rev. B* **2023**, *107*, 035112. [[CrossRef](#)]
33. Zhong, D.; Seyler, K.L.; Linpeng, X.; Cheng, R.; Sivadas, N.; Huang, B.; Schmidgall, E.; Taniguchi, T.; Watanabe, K.; McGuire, M.A.; et al. Van der Waals engineering of ferromagnetic semiconductor heterostructures for spin and valleytronics. *Sci. Adv.* **2017**, *3*, e1603113. [[CrossRef](#)] [[PubMed](#)]
34. Ciorciaro, L.; Kroner, M.; Watanabe, K.; Taniguchi, T.; Imamoglu, A. Observation of magnetic proximity effect using resonant optical spectroscopy of an electrically tunable MoSe₂/CrBr₃ heterostructure. *Phys. Rev. Lett.* **2020**, *124*, 197401. [[CrossRef](#)] [[PubMed](#)]
35. Choi, J.; Lane, C.; Zhu, J.X.; Crooker, S.A. Asymmetric magnetic proximity interactions in MoSe₂/CrBr₃ van der Waals heterostructures. *Nat. Mater.* **2022**, *22*, 305–310. [[CrossRef](#)] [[PubMed](#)]
36. Chaves, A.; Azadani, J.G.; Özçelik, V.O.; Grassi, R.; Low, T. Electrical control of excitons in van der Waals heterostructures with type-II band alignment. *Phys. Rev. B* **2018**, *98*, 121302. [[CrossRef](#)]
37. Gillen, R.; Maultzsch, J. Interlayer excitons in MoSe₂/WSe₂ heterostructures from first principles. *Phys. Rev. B* **2018**, *97*, 165306. [[CrossRef](#)]
38. Torun, E.; Miranda, H.P.C.; Molina-Sánchez, A.; Wirtz, L. Interlayer and intralayer excitons in MoS₂/WS₂ and MoSe₂/WSe₂ heterobilayers. *Phys. Rev. B* **2018**, *97*, 245427. [[CrossRef](#)]
39. Rivera, P.; Schaibley, J.R.; Jones, A.M.; Ross, J.S.; Wu, S.; Aivazian, G.; Klement, P.; Seyler, K.; Clark, G.; Ghimire, N.J.; et al. Observation of long-lived interlayer excitons in monolayer MoSe₂-WSe₂ heterostructures. *Nat. Commun.* **2015**, *6*, 6242. [[CrossRef](#)]
40. Miller, B.; Steinhoff, A.; Pano, B.; Klein, J.; Jahnke, F.; Holleitner, A.; Wurstbauer, U. Long-Lived Direct and Indirect Interlayer Excitons in van der Waals Heterostructures. *Nano Lett.* **2017**, *17*, 5229. [[CrossRef](#)]
41. Nagler, P.; Plechinger, G.; Ballottin, M.V.; Mitioglu, A.; Meier, S.; Paradiso, N.; Strunk, C.; Chernikov, A.; Christianen, P.C.M.; Schüller, C.; et al. Interlayer exciton dynamics in a dichalcogenide monolayer heterostructure. *2D Mater.* **2017**, *4*, 025112. [[CrossRef](#)]
42. Ciarrocchi, A.; Unuchek, D.; Avsar, A.; Watanabe, K.; Taniguchi, T.; Kis, A. Polarization switching and electrical control of interlayer excitons in two-dimensional van der Waals heterostructures. *Nat. Photonics* **2019**, *13*, 131. [[CrossRef](#)]
43. Baek, H.; Brotons-Gisbert, M.; Koong, Z.X.; Campbell, A.; Rambach, M.; Watanabe, K.; Taniguchi, T.; Gerardot, B.D. Highly energy-tunable quantum light from moiré-trapped excitons. *Sci. Adv.* **2020**, *6*, eaba8526. [[CrossRef](#)] [[PubMed](#)]
44. Shanks, D.N.; Mahdikhanyarvejahany, F.; Mucciante, C.; Alfrey, A.; Koehler, M.R.; Mandrus, D.G.; Taniguchi, T.; Watanabe, K.; Yu, H.; LeRoy, B.J.; et al. Nanoscale Trapping of Interlayer Excitons in a 2D Semiconductor Heterostructure. *Nano Lett.* **2021**, *21*, 5641. [[CrossRef](#)] [[PubMed](#)]
45. Barré, E.; Karni, O.; Liu, E.; O’Beirne, A.L.; Chen, X.; Ribeiro, H.B.; Yu, L.; Kim, B.; Watanabe, K.; Taniguchi, T.; et al. Optical absorption of interlayer excitons in transition-metal dichalcogenide heterostructures. *Science* **2022**, *376*, 406. [[CrossRef](#)]
46. Shanks, D.N.; Mahdikhanyarvejahany, F.; Stanfill, T.G.; Koehler, M.R.; Mandrus, D.G.; Taniguchi, T.; Watanabe, K.; LeRoy, B.J.; Schaibley, J.R. Interlayer Exciton Diode and Transistor. *Nano Lett.* **2022**, *22*, 6599. [[CrossRef](#)] [[PubMed](#)]
47. Nagler, P.; Ballottin, M.V.; Mitioglu, A.A.; Mooshammer, F.; Paradiso, N.; Strunk, C.; Huber, R.; Chernikov, A.; Christianen, P.C.M.; Schüller, C.; et al. Giant magnetic splitting inducing near-unity valley polarization in van der Waals heterostructures. *Nat. Commun.* **2017**, *8*, 1551. [[CrossRef](#)]
48. Mahdikhanyarvejahany, F.; Shanks, D.N.; Mucciante, C.; Badada, B.H.; Idi, I.; Alfrey, A.; Raglow, S.; Koehler, M.R.; Mandrus, D.G.; Taniguchi, T.; et al. Temperature dependent moiré trapping of interlayer excitons in MoSe₂-WSe₂ heterostructures. *Npj 2D Mater. Appl.* **2021**, *5*, 67. [[CrossRef](#)]
49. Holler, J.; Selig, M.; Kempf, M.; Zipfel, J.; Nagler, P.; Katzer, M.; Katsch, F.; Ballottin, M.V.; Mitioglu, A.A.; Chernikov, A.; et al. Interlayer exciton valley polarization dynamics in large magnetic fields. *Phys. Rev. B* **2022**, *105*, 085303. [[CrossRef](#)]
50. Smirnov, D.S.; Holler, J.; Kempf, M.; Zipfel, J.; Nagler, P.; Ballottin, M.V.; Mitioglu, A.A.; Chernikov, A.; Christianen, P.C.M.; Schüller, C.; et al. Valley-magnetophonon resonance for interlayer excitons. *2D Mater.* **2022**, *9*, 045016. [[CrossRef](#)]
51. Li, Z.; Tabataba-Vakili, F.; Zhao, S.; Rupp, A.; Bilgin, I.; Herdegen, Z.; März, B.; Watanabe, K.; Taniguchi, T.; Schleder, G.R.; et al. Lattice reconstruction in MoSe₂-WSe₂ heterobilayers synthesized by chemical vapor deposition. *arXiv* **2022**, arXiv:2212.07686.
52. Choi, J.; Florian, M.; Steinhoff, A.; Erben, D.; Tran, K.; Kim, D.S.; Sun, L.; Quan, J.; Claassen, R.; Majumder, S.; et al. Twist Angle-Dependent Interlayer Exciton Lifetimes in van der Waals Heterostructures. *Phys. Rev. Lett.* **2021**, *126*, 047401. [[CrossRef](#)]
53. Förg, M.; Baimuratov, A.S.; Kruchinin, S.Y.; Vovk, I.A.; Scherzer, J.; Förste, J.; Funk, V.; Watanabe, K.; Taniguchi, T.; Högele, A. Moiré excitons in MoSe₂-WSe₂ heterobilayers and heterotrilayers. *Nat. Commun.* **2021**, *12*, 1656. [[CrossRef](#)] [[PubMed](#)]
54. Enaldiev, V.V.; Zólyomi, V.; Yelgel, C.; Magorrian, S.J.; Fal’ko, V.I. Stacking Domains and Dislocation Networks in Marginally Twisted Bilayers of Transition Metal Dichalcogenides. *Phys. Rev. Lett.* **2020**, *124*, 206101. [[CrossRef](#)]

55. Holler, J.; Meier, S.; Kempf, M.; Nagler, P.; Watanabe, K.; Taniguchi, T.; Korn, T.; Schüller, C. Low-frequency Raman scattering in WSe₂-MoSe₂ heterobilayers: Evidence for atomic reconstruction. *Appl. Phys. Lett.* **2020**, *117*, 013104. [[CrossRef](#)]
56. Parzefall, P.; Holler, J.; Scheuck, M.; Beer, A.; Lin, K.Q.; Peng, B.; Monserrat, B.; Nagler, P.; Kempf, M.; Korn, T.; et al. Moiré phonons in twisted MoSe₂-WSe₂ heterobilayers and their correlation with interlayer excitons. *2D Mater.* **2021**, *8*, 035030. [[CrossRef](#)]
57. Zhao, S.; Huang, X.; Li, Z.; Rupp, A.; Göser, J.; Vovk, I.A.; Kruchinin, S.Y.; Watanabe, K.; Taniguchi, T.; Bilgin, I.; et al. Excitons in mesoscopically reconstructed moiré heterostructures. *arXiv* **2022**, arXiv:2202.11139.
58. Hanbicki, A.T.; Chuang, H.J.; Rosenberger, M.R.; Hellberg, C.S.; Sivaram, S.V.; McCreary, K.M.; Mazin, I.I.; Jonker, B.T. Double Indirect Interlayer Exciton in a MoSe₂/WSe₂ van der Waals Heterostructure. *ACS Nano* **2018**, *12*, 4719. [[CrossRef](#)]
59. Sigl, L.; Sigger, F.; Kronowetter, F.; Kiemle, J.; Klein, J.; Watanabe, K.; Taniguchi, T.; Finley, J.J.; Wurstbauer, U.; Holleitner, A.W. Signatures of a degenerate many-body state of interlayer excitons in a van der Waals heterostack. *Phys. Rev. Res.* **2020**, *2*, 042044. [[CrossRef](#)]
60. Wang, T.; Miao, S.; Li, Z.; Meng, Y.; Lu, Z.; Lian, Z.; Blei, M.; Taniguchi, T.; Watanabe, K.; Tongay, S.; et al. Giant Valley-Zeeman Splitting from Spin-Singlet and Spin-Triplet Interlayer Excitons in WSe₂/MoSe₂ Heterostructure. *Nano Lett.* **2020**, *20*, 694. [[CrossRef](#)]
61. Delhomme, A.; Vaclavkova, D.; Slobodeniuk, A.; Orlita, M.; Potemski, M.; Basko, D.M.; Watanabe, K.; Taniguchi, T.; Mauro, D.; Barreateau, C.; et al. Flipping exciton angular momentum with chiral phonons in MoSe₂/WSe₂ heterobilayers. *2D Mater.* **2020**, *7*, 041002. [[CrossRef](#)]
62. Ramasubramaniam, A.; Naveh, D.; Towe, E. Tunable band gaps in bilayer transition-metal dichalcogenides. *Phys. Rev. B* **2011**, *84*, 205325. [[CrossRef](#)]
63. Plankl, M.; Faria Junior, P.E.; Mooshammer, F.; Siday, T.; Zizlsperger, M.; Sandner, F.; Schiegl, F.; Maier, S.; Huber, M.A.; Gmitra, M.; et al. Subcycle contact-free nanoscopy of ultrafast interlayer transport in atomically thin heterostructures. *Nat. Photonics* **2021**, *15*, 594. [[CrossRef](#)]
64. Woźniak, T.; Faria Junior, P.E.; Seifert, G.; Chaves, A.; Kunstmann, J. Exciton g factors of van der Waals heterostructures from first-principles calculations. *Phys. Rev. B* **2020**, *101*, 235408. [[CrossRef](#)]
65. Deilmann, T.; Krüger, P.; Rohlfing, M. Ab Initio Studies of Exciton g Factors: Monolayer Transition Metal Dichalcogenides in Magnetic Fields. *Phys. Rev. Lett.* **2020**, *124*, 226402. [[CrossRef](#)]
66. Förste, J.; Tepliakov, N.V.; Kruchinin, S.Y.; Lindlau, J.; Funk, V.; Förg, M.; Watanabe, K.; Taniguchi, T.; Baimuratov, A.S.; Högele, A. Exciton g-factors in monolayer and bilayer WSe₂ from experiment and theory. *Nat. Commun.* **2020**, *11*, 4539. [[CrossRef](#)]
67. Xuan, F.; Quek, S.Y. Valley Zeeman effect and Landau levels in two-dimensional transition metal dichalcogenides. *Phys. Rev. Res.* **2020**, *2*, 033256. [[CrossRef](#)]
68. Yu, H.; Wang, Y.; Tong, Q.; Xu, X.; Yao, W. Anomalous Light Cones and Valley Optical Selection Rules of Interlayer Excitons in Twisted Heterobilayers. *Phys. Rev. Lett.* **2015**, *115*, 187002. [[CrossRef](#)]
69. Yu, H.; Liu, G.B.; Tang, J.; Xu, X.; Yao, W. Moiré excitons: From programmable quantum emitter arrays to spin-orbit-coupled artificial lattices. *Sci. Adv.* **2017**, *3*, e1701696. [[CrossRef](#)]
70. Nieken, R.; Roche, A.; Mahdikhanyarvejahany, F.; Taniguchi, T.; Watanabe, K.; Koehler, M.R.; Mandrus, D.G.; Schaibley, J.; LeRoy, B.J. Direct STM measurements of R-type and H-type twisted MoSe₂/WSe₂. *APL Mater.* **2022**, *10*, 031107. [[CrossRef](#)]
71. Wu, F.; Lovorn, T.; MacDonald, A.H. Topological Exciton Bands in Moiré Heterojunctions. *Phys. Rev. Lett.* **2017**, *118*, 147401. [[CrossRef](#)] [[PubMed](#)]
72. Yu, H.; Liu, G.B.; Yao, W. Brightened spin-triplet interlayer excitons and optical selection rules in van der Waals heterobilayers. *2D Mater.* **2018**, *5*, 035021. [[CrossRef](#)]
73. Wu, F.; Lovorn, T.; MacDonald, A.H. Theory of optical absorption by interlayer excitons in transition metal dichalcogenide heterobilayers. *Phys. Rev. B* **2018**, *97*, 035306. [[CrossRef](#)]
74. Ruiz-Tijerina, D.A.; Soltero, I.; Mireles, F. Theory of moiré localized excitons in transition metal dichalcogenide heterobilayers. *Phys. Rev. B* **2020**, *102*, 195403. [[CrossRef](#)]
75. Erkensten, D.; Brem, S.; Malic, E. Exciton-exciton interaction in transition metal dichalcogenide monolayers and van der Waals heterostructures. *Phys. Rev. B* **2021**, *103*, 045426. [[CrossRef](#)]
76. Kormányos, A.; Burkard, G.; Gmitra, M.; Fabian, J.; Zólyomi, V.; Drummond, N.D.; Fal'ko, V. k·p theory for two-dimensional transition metal dichalcogenide semiconductors. *2D Mater.* **2015**, *2*, 022001. [[CrossRef](#)]
77. Zollner, K.; Faria Junior, P.E.; Fabian, J. Strain-tunable orbital, spin-orbit, and optical properties of monolayer transition-metal dichalcogenides. *Phys. Rev. B* **2019**, *100*, 195126. [[CrossRef](#)]
78. Nayak, P.K.; Horbatenko, Y.; Ahn, S.; Kim, G.; Lee, J.U.; Ma, K.Y.; Jang, A.R.; Lim, H.; Kim, D.; Ryu, S.; et al. Probing evolution of twist-angle-dependent interlayer excitons in MoSe₂/WSe₂ van der Waals heterostructures. *ACS Nano* **2017**, *11*, 4041. [[CrossRef](#)]
79. Xu, K.; Xu, Y.; Zhang, H.; Peng, B.; Shao, H.; Ni, G.; Li, J.; Yao, M.; Lu, H.; Zhu, H.; et al. The role of Anderson's rule in determining electronic, optical and transport properties of transition metal dichalcogenide heterostructures. *Phys. Chem. Chem. Phys.* **2018**, *20*, 30351. [[CrossRef](#)]
80. Gillen, R. Interlayer Excitonic Spectra of Vertically Stacked MoSe₂/WSe₂ Heterobilayers. *Phys. Status Solidi (b)* **2021**, *258*, 2000614. [[CrossRef](#)]

81. Blaha, P.; Schwarz, K.; Tran, F.; Laskowski, R.; Madsen, G.K.; Marks, L.D. WIEN2k: An APW+lo program for calculating the properties of solids. *J. Chem. Phys.* **2020**, *152*, 074101. [[CrossRef](#)]
82. Song, Y.; Dery, H. Transport Theory of Monolayer Transition-Metal Dichalcogenides through Symmetry. *Phys. Rev. Lett.* **2013**, *111*, 026601. [[CrossRef](#)]
83. Dery, H.; Song, Y. Polarization analysis of excitons in monolayer and bilayer transition-metal dichalcogenides. *Phys. Rev. B* **2015**, *92*, 125431. [[CrossRef](#)]
84. Gilardoni, C.M.; Hendriks, F.; van der Wal, C.H.; Guimarães, M.H.D. Symmetry and control of spin-scattering processes in two-dimensional transition metal dichalcogenides. *Phys. Rev. B* **2021**, *103*, 115410. [[CrossRef](#)]
85. Blundo, E.; Faria Junior, P.E.; Surrente, A.; Pettinari, G.; Prosnikov, M.A.; Olkowska-Pucko, K.; Zollner, K.; Woźniak, T.; Chaves, A.; Kazimierzczuk, T.; et al. Strain-Induced Exciton Hybridization in WS₂ Monolayers Unveiled by Zeeman-Splitting Measurements. *Phys. Rev. Lett.* **2022**, *129*, 067402. [[CrossRef](#)]
86. Dresselhaus, G. Spin-Orbit Coupling Effects in Zinc Blende Structures. *Phys. Rev.* **1955**, *100*, 580. [[CrossRef](#)]
87. Kane, E.O. *Physics of III-V Compounds; Semiconductors and Semimetals*; Academic Press: New York, NY, USA, 1966; Volume 1. [[CrossRef](#)]
88. Kane, E.O. Band structure of indium antimonide. *J. Phys. Chem. Solids* **1957**, *1*, 249. [[CrossRef](#)]
89. Dresselhaus, M.S.; Dresselhaus, G.; Jorio, A. *Group Theory: Application to the Physics of Condensed Matter*; Springer Science & Business Media: Berlin/Heidelberg, Germany, 2007.
90. Lew Yan Voon, L.C.; Willatzen, M. *The k.p Method: Electronic Properties of Semiconductors*; Springer: Berlin, Germany, 2009.
91. Koster, G.F.; Dimmock, J.O.; Wheeler, R.G.; Statz, H. *Properties of the Thirty-Two Point Groups*; MIT Press: Cambridge, MA, USA, 1963; Volume 24.
92. Xuan, F.; Quek, S.Y. Valley-filling instability and critical magnetic field for interaction-enhanced Zeeman response in doped WSe₂ monolayers. *Npj Comput. Mater.* **2021**, *7*, 198. [[CrossRef](#)]
93. Heißenbüttel, M.C.; Deilmann, T.; Krüger, P.; Rohlfing, M. Valley-Dependent Interlayer Excitons in Magnetic WSe₂/CrI₃. *Nano Lett.* **2021**, *21*, 5173–5178. [[CrossRef](#)]
94. Covre, F.S.; Faria Junior, P.E.; Gordo, V.O.; de Brito, C.S.; Zhumagulov, Y.V.; Teodoro, M.D.; Couto, O.D.D.; Misoguti, L.; Pratavieira, S.; Andrade, M.B.; et al. Revealing the impact of strain in the optical properties of bubbles in monolayer MoSe₂. *Nanoscale* **2022**, *14*, 5758. [[CrossRef](#)] [[PubMed](#)]
95. Faria Junior, P.E.; Zollner, K.; Woźniak, T.; Kurpas, M.; Gmitra, M.; Fabian, J. First-principles insights into the spin-valley physics of strained transition metal dichalcogenides monolayers. *New J. Phys.* **2022**, *24*, 083004. [[CrossRef](#)]
96. Raiber, S.; Faria Junior, P.E.; Falter, D.; Feldl, S.; Marzena, P.; Watanabe, K.; Taniguchi, T.; Fabian, J.; Schüller, C. Ultrafast pseudospin quantum beats in multilayer WSe₂ and MoSe₂. *Nat. Commun.* **2022**, *13*, 4997. [[CrossRef](#)] [[PubMed](#)]
97. Amit, T.; Hernangómez-Pérez, D.; Cohen, G.; Qiu, D.Y.; Refaely-Abramson, S. Tunable magneto-optical properties in MoS₂ via defect-induced exciton transitions. *Phys. Rev. B* **2022**, *106*, L161407. [[CrossRef](#)]
98. Hötger, A.; Amit, T.; Klein, J.; Barthelmi, K.; Pelini, T.; Delhomme, A.; Rey, S.; Potemski, M.; Faugeras, C.; Cohen, G.; et al. Spin-defect characteristics of single sulfur vacancies in monolayer MoS₂. *arXiv* **2022**, arXiv:2205.10286.
99. Gobato, Y.G.; de Brito, C.S.; Chaves, A.; Prosnikov, M.A.; Woźniak, T.; Guo, S.; Barcelos, I.D.; Milošević, M.V.; Withers, F.; Christianen, P.C.M. Distinctive g-Factor of Moiré-Confined Excitons in van der Waals Heterostructures. *Nano Lett.* **2022**, *22*, 8641. [[CrossRef](#)]
100. Lejaeghere, K.; Bihlmayer, G.; Björkman, T.; Blaha, P.; Blügel, S.; Blum, V.; Caliste, D.; Castelli, I.E.; Clark, S.J.; Corso, A.D.; et al. Reproducibility in density functional theory calculations of solids. *Science* **2016**, *351*, aad3000. [[CrossRef](#)]
101. Gmitra, M.; Konshuh, S.; Ertler, C.; Ambrosch-Draxl, C.; Fabian, J. Band-structure topologies of graphene: Spin-orbit coupling effects from first principles. *Phys. Rev. B* **2009**, *80*, 235431. [[CrossRef](#)]
102. Konshuh, S.; Gmitra, M.; Fabian, J. Tight-binding theory of the spin-orbit coupling in graphene. *Phys. Rev. B* **2010**, *82*, 245412. [[CrossRef](#)]
103. Kurpas, M.; Gmitra, M.; Fabian, J. Spin-orbit coupling and spin relaxation in phosphorene: Intrinsic versus extrinsic effects. *Phys. Rev. B* **2016**, *94*, 155423. [[CrossRef](#)]
104. Kurpas, M.; Faria Junior, P.E.; Gmitra, M.; Fabian, J. Spin-orbit coupling in elemental two-dimensional materials. *Phys. Rev. B* **2019**, *100*, 125422. [[CrossRef](#)]
105. Faria Junior, P.E.; Kurpas, M.; Gmitra, M.; Fabian, J. *k.p* theory for phosphorene: Effective g-factors, Landau levels, and excitons. *Phys. Rev. B* **2019**, *100*, 115203. [[CrossRef](#)]
106. Fülöp, B.; Márffy, A.; Zihlmann, S.; Gmitra, M.; Tóvári, E.; Szentpéteri, B.; Kedves, M.; Watanabe, K.; Taniguchi, T.; Fabian, J.; et al. Boosting proximity spin-orbit coupling in graphene/WSe₂ heterostructures via hydrostatic pressure. *Npj 2D Mater. Appl.* **2021**, *5*, 82. [[CrossRef](#)]
107. Oliva, R.; Woźniak, T.; Faria Junior, P.E.; Dybala, F.; Kopaczek, J.; Fabian, J.; Scharoch, P.; Kudrawiec, R. Strong Substrate Strain Effects in Multilayered WS₂ Revealed by High-Pressure Optical Measurements. *ACS Appl. Mater. Interfaces* **2022**, *14*, 19857. [[CrossRef](#)] [[PubMed](#)]
108. Koo, Y.; Lee, H.; Ivanova, T.; Kefayati, A.; Perebeinos, V.; Khestanova, E.; Kravtsov, V.; Park, K.D. Tunable interlayer excitons and switchable interlayer trions via dynamic near-field cavity. *Light. Sci. Appl.* **2023**, *12*, 59. [[CrossRef](#)] [[PubMed](#)]

109. Kunstmann, J.; Mooshammer, F.; Nagler, P.; Chaves, A.; Stein, F.; Paradiso, N.; Plechinger, G.; Strunk, C.; Schüller, C.; Seifert, G.; et al. Momentum-space indirect interlayer excitons in transition-metal dichalcogenide van der Waals heterostructures. *Nat. Phys.* **2018**, *14*, 801. [[CrossRef](#)]
110. Robert, C.; Dery, H.; Ren, L.; Van Tuan, D.; Courtade, E.; Yang, M.; Urbaszek, B.; Lagarde, D.; Watanabe, K.; Taniguchi, T.; et al. Measurement of Conduction and Valence Bands g-Factors in a Transition Metal Dichalcogenide Monolayer. *Phys. Rev. Lett.* **2021**, *126*, 067403. [[CrossRef](#)]
111. Zinkiewicz, M.; Woźniak, T.; Kazimierczuk, T.; Kapuscinski, P.; Oreszczuk, K.; Grzeszczyk, M.; Bartoš, M.; Nogajewski, K.; Watanabe, K.; Taniguchi, T.; et al. Excitonic Complexes in n-Doped WS₂ Monolayer. *Nano Lett.* **2021**, *21*, 2519. [[CrossRef](#)]
112. Robert, C.; Amand, T.; Cadiz, F.; Lagarde, D.; Courtade, E.; Manca, M.; Taniguchi, T.; Watanabe, K.; Urbaszek, B.; Marie, X. Fine structure and lifetime of dark excitons in transition metal dichalcogenide monolayers. *Phys. Rev. B* **2017**, *96*, 155423. [[CrossRef](#)]
113. Molas, M.R.; Slobodeniuk, A.O.; Kazimierczuk, T.; Nogajewski, K.; Bartos, M.; Kapuściński, P.; Oreszczuk, K.; Watanabe, K.; Taniguchi, T.; Faugeras, C.; et al. Probing and Manipulating Valley Coherence of Dark Excitons in Monolayer WSe₂. *Phys. Rev. Lett.* **2019**, *123*, 096803. [[CrossRef](#)]
114. Zinkiewicz, M.; Slobodeniuk, A.; Kazimierczuk, T.; Kapuściński, P.; Oreszczuk, K.; Grzeszczyk, M.; Bartos, M.; Nogajewski, K.; Watanabe, K.; Taniguchi, T.; et al. Neutral and charged dark excitons in monolayer WS₂. *Nanoscale* **2020**, *12*, 18153. [[CrossRef](#)]
115. Inui, T.; Tanabe, Y.; Onodera, Y. *Group Theory and Its Applications in Physics*; Springer Science & Business Media: Berlin/Heidelberg, Germany, 2012; Volume 78.
116. Joe, A.Y.; Jauregui, L.A.; Pistunova, K.; Mier Valdivia, A.M.; Lu, Z.; Wild, D.S.; Scuri, G.; De Greve, K.; Gelly, R.J.; Zhou, Y.; et al. Electrically controlled emission from singlet and triplet exciton species in atomically thin light-emitting diodes. *Phys. Rev. B* **2021**, *103*, L161411. [[CrossRef](#)]
117. Qian, C.; Troue, M.; Figueiredo, J.; Soubelet, P.; Villafaña, V.; Beierlein, J.; Klemmt, S.; Stier, A.V.; Höfling, S.; Holleitner, A.W.; et al. Lasing of Moiré Trapped MoSe₂/WSe₂ Interlayer Excitons Coupled to a Nanocavity. *arXiv* **2023**, arXiv:2302.07046.
118. Roch, J.G.; Leisgang, N.; Froehlicher, G.; Makk, P.; Watanabe, K.; Taniguchi, T.; Schönenberger, C.; Warburton, R.J. Quantum-Confined Stark Effect in a MoS₂. *Nano Lett.* **2018**, *18*, 1070. [[CrossRef](#)] [[PubMed](#)]
119. Chakraborty, C.; Mukherjee, A.; Qiu, L.; Vamivakas, A.N. Electrically tunable valley polarization and valley coherence in monolayer WSe₂. *Opt. Mater. Express* **2019**, *9*, 1479. [[CrossRef](#)]
120. Altaïary, M.M.; Liu, E.; Liang, C.T.; Hsiao, F.C.; van Baren, J.; Taniguchi, T.; Watanabe, K.; Gabor, N.M.; Chang, Y.C.; Lui, C.H. Electrically Switchable Intervalley Excitons with Strong Two-Phonon Scattering in Bilayer WSe₂. *Nano Lett.* **2022**, *22*, 1829. [[CrossRef](#)]
121. Huang, Z.; Zhao, Y.; Bo, T.; Chu, Y.; Tian, J.; Liu, L.; Yuan, Y.; Wu, F.; Zhao, J.; Xian, L.; et al. Spatially indirect intervalley excitons in bilayer WSe₂. *Phys. Rev. B* **2022**, *105*, L041409. [[CrossRef](#)]
122. Glazov, M.M.; Amand, T.; Marie, X.; Lagarde, D.; Bouet, L.; Urbaszek, B. Exciton fine structure and spin decoherence in monolayers of transition metal dichalcogenides. *Phys. Rev. B* **2014**, *89*, 201302. [[CrossRef](#)]
123. Glazov, M.M.; Ivchenko, E.L.; Wang, G.; Amand, T.; Marie, X.; Urbaszek, B.; Liu, B. Spin and valley dynamics of excitons in transition metal dichalcogenide monolayers. *Phys. Status Solidi (b)* **2015**, *252*, 2349. [[CrossRef](#)]
124. Feng, S.; Campbell, A.; Brotons-Gisbert, M.; Baek, H.; Watanabe, K.; Taniguchi, T.; Urbaszek, B.; Gerber, I.C.; Gerardot, B.D. Highly Tunable Ground and Excited State Excitonic Dipoles in Multilayer 2H-MoSe₂. *arXiv* **2022**, arXiv:2212.14338.
125. Deilmann, T.; Thygesen, K.S. Interlayer Excitons with Large Optical Amplitudes in Layered van der Waals Materials. *Nano Lett.* **2018**, *18*, 2984. [[CrossRef](#)]
126. McDonnell, L.P.; Viner, J.J.; Rivera, P.; Cammarata, A.; Sen, H.S.; Xu, X.; Smith, D.C. Experimental realisation of Dual Periodicity Moiré Superlattice in a MoSe₂/WSe₂ Heterobilayer. *arXiv* **2020**, arXiv:2009.07676.
127. Volmer, F.; Ersfeld, M.; Faria Junior, P.E.; Waldecker, L.; Parashar, B.; Rathmann, L.; Dubey, S.; Cojocariu, I.; Feyer, V.; Watanabe, K.; et al. Twist angle dependent interlayer transfer of valley polarization from excitons to free charge carriers in WSe₂/MoSe₂ heterobilayers. *arXiv* **2022**, arXiv:2211.17210.
128. Li, W.; Devenica, L.M.; Zhang, J.; Zhang, Y.; Lu, X.; Watanabe, K.; Taniguchi, T.; Rubio, A.; Srivastava, A. Local Sensing of Correlated Electrons in Dual-moiré Heterostructures using Dipolar Excitons. *arXiv* **2021**, arXiv:2111.09440.
129. Zhang, Y.; Xiao, C.; Ovchinnikov, D.; Zhu, J.; Wang, X.; Taniguchi, T.; Watanabe, K.; Yan, J.; Yao, W.; Xu, X. Every-other-layer Dipolar Excitons in a Spin-Valley locked Superlattice. *arXiv* **2022**, arXiv:2212.14140.
130. Alexeev, E.M.; Ruiz-Tijerina, D.A.; Danovich, M.; Hamer, M.J.; Terry, D.J.; Nayak, P.K.; Ahn, S.; Pak, S.; Lee, J.; Sohn, J.I.; et al. Resonantly hybridized excitons in moiré superlattices in van der Waals heterostructures. *Nature* **2019**, *567*, 81. [[CrossRef](#)] [[PubMed](#)]
131. Tang, Y.; Gu, J.; Liu, S.; Watanabe, K.; Taniguchi, T.; Hone, J.; Mak, K.F.; Shan, J. Tuning layer-hybridized moiré excitons by the quantum-confined Stark effect. *Nat. Nanotechnol.* **2020**, *16*, 52. [[CrossRef](#)]
132. Bahn, S.R.; Jacobsen, K.W. An object-oriented scripting interface to a legacy electronic structure code. *Comput. Sci. Eng.* **2002**, *4*, 56. [[CrossRef](#)]
133. Perdew, J.P.; Burke, K.; Ernzerhof, M. Generalized Gradient Approximation Made Simple. *Phys. Rev. Lett.* **1996**, *77*, 3865. [[CrossRef](#)] [[PubMed](#)]
134. Grimme, S.; Antony, J.; Ehrlich, S.; Krieg, H. A consistent and accurate ab initio parametrization of density functional dispersion correction (DFT-D) for the 94 elements H-Pu. *J. Chem. Phys.* **2010**, *132*, 154104. [[CrossRef](#)] [[PubMed](#)]

135. Singh, D.J.; Nordstrom, L. *Planewaves, Pseudopotentials, and the LAPW Method*; Springer Science & Business Media: Berlin/Heidelberg, Germany, 2006.
136. Stahn, J.; Pietsch, U.; Blaha, P.; Schwarz, K. Electric-field-induced charge-density variations in covalently bonded binary compounds. *Phys. Rev. B* **2001**, *63*, 165205. [[CrossRef](#)]

Disclaimer/Publisher's Note: The statements, opinions and data contained in all publications are solely those of the individual author(s) and contributor(s) and not of MDPI and/or the editor(s). MDPI and/or the editor(s) disclaim responsibility for any injury to people or property resulting from any ideas, methods, instructions or products referred to in the content.